석 사 학 위 논 문

Master's Thesis

근적외선 분광신호와 기능자기공명영상의 동시측정 및 통계처리를 위한 Statistical Parametric Mapping Toolbox 개발

Development of Statistical Parametric Mapping Toolbox for Near Infrared Spectroscopy

KOREA ADVANCED INSTITUTE OF SCIENCE AND TECHNOLOGY
KAIST
한국과학기술원
SINCE 1971

탁 성 호 (卓 成 昊 Tak, Sungho)

바이오및뇌공학과

Department of Bio and Brain Engineering

한 국 과 학 기 술 원

Korea Advanced Institute of Science and Technology

2008

근적외선 분광신호와 기능자기공명영상의 동시측정 및 통계처리를 위한 Statistical Parametric Mapping Toolbox 개발

Development of Statistical Parametric Mapping Toolbox for Near Infrared Spectroscopy

KAIST

Development of Statistical Parametric Mapping Toolbox for Near Infrared Spectroscopy

Advisor : Professor Jong Chul Ye

by

Tak, Sungho
Department of Bio and Brain Engineering
Korea Advanced Institute of Science and Technology

KAIST

A thesis submitted to the faculty of the Korea Advanced Institute of Science and Technology in partial fulfillment of the requirements for the degree of Master of Science in the Department of Bio and Brain Engineering

Daejeon, Korea
2007. 12. 27.
Approved by

Professor Jong Chul Ye
Advisor

근적외선 분광신호와 기능자기공명영상의 동시측정 및 통계처리를 위한 Statistical Parametric Mapping Toolbox 개발

탁 성 호

위 논문은 한국과학기술원 석사학위논문으로 학위논문심사 위원회에서 심사 통과하였음.

KAIST

2007년 12월 27일

심사위원장 예 종 철 (인)

심사위원 이 수 영 (인)

심사위원 박 현 욱 (인)

MBiB
20063600

탁 성 호. Tak, Sungho. Development of Statistical Parametric Mapping Toolbox for Near Infrared Spectroscopy. 근적외선 분광신호와 기능자기공명영상의 동시측정 및 통계처리를 위한 Statistical Parametric Mapping Toolbox 개발. Department of Bio and Brain Engineering . 2008. 41p. Advisor Prof. Jong Chul Ye. Text in English.

Abstract

Even though there exists a powerful statistical parametric mapping (SPM) tool for functional magnetic resonance imaging (fMRI), similar public domain tools are not available for near infrared spectroscopy (NIRS). In this paper, we describe a new public domain statistical toolbox called NIRS-SPM for quantitative analysis of NIRS signals. Mainly, NIRS-SPM statistically analyzes the NIRS data using general linear model (GLM) and makes inferences as the excursion probability which comes from inhomogeneous Gaussian random field that are interpolated from the spare measurement. In order to obtain the correct inference, NIRS-SPM offers the pre-coloring and pre-whitening method for temporal correlation estimation. For simultaneous recording NIRS with fMRI, the spatial mapping between fMRI images and real coordinates in 3-D digitizer is estimated using Horn's algorithm. These powerful tools allow us the super-resolution localization of the brain activation which is not possible using the conventional NIRS analysis tools.

KAIST

Contents

Abstract i

Contents iii

List of Tables v

List of Figures vi

1 Introduction 1

2 A Brief Review of SPM 4

2.1 General Linear Model 4

2.2 Gaussian Random Field Theory 6

3 Statistical Parametric Mapping for Near Infrared Spectroscopy 7

3.1 Measurement Model for NIRS 7

3.2 General Linear Model for NIRS 8

3.3 Inference using Global Confidence Region Analysis 10

3.3.1 One-side t-test for HbO_2 or HbR 12

3.3.2 Two side t-test for both HbO_2 and HbR 14

3.4 Temporal Preprocessing: Detrending and Estimating the Temporal Correlations. 15

3.5 Spatial Preprocessing: NIRS-fMRI Alignment 16

4 NIRS-SPM: a New SPM Toolbox for NIRS 18

5 Experimental Results 20

5.1 Subject 20

5.2 Data Acquisition 20

5.3 Behavior Protocol 20

5.4 Results 21

KAIST

5.4.1 Right Finger Tapping 23
5.4.2 Working Memory Task 30

6 Conclusion **37**

Summary (in Korean) **38**

References **39**

KAIST

List of Tables

KAIST

List of Figures

3.1 The difference between fMRI and NIRS model. 11

4.1 Main panel of the NIRS-SPM showing the four main groups of tools. 18
4.2 Schematic describing the NIRS-SPM framework 19

5.1 Schematic diagram of the 24 NIRS channels. Red circles are illuminators. Blue circles are detectors. Numbers between red and blue circles are NIRS channels. 21
5.2 (a) The holder cap of 16 optodes covering the primary motor cortex and Broca's area, (b) 24 NIRS channels onto the SPM brain template. 22
5.3 Estimated trend of (a) NIRS and (b) fMRI signal. Blue line: (a) NIRS and (b) fMRI time series, red line: the estimated bias based on the DCT method. 22
5.4 T-statistic maps from ΔHbO_2 using (a) pre-whitening, fOSA [7], (b) pre-coloring, fOSA, (c) pre-whitening, NIRS-SPM, and (d) pre-coloring, NIRS-SPM. 23
5.5 T-statistic maps from ΔHbR using (a) pre-whitening, fOSA, (b) pre-coloring, fOSA, (c) pre-whitening, NIRS-SPM, and (d) pre-coloring, NIRS-SPM. . . . 24
5.6 T-statistic maps from both ΔHbO_2 and ΔHbR using (a) pre-whitening, fOSA, (b) pre-coloring, fOSA, (c) pre-whitening, NIRS-SPM, and (d) pre-coloring, NIRS-SPM. 25
5.7 SPM analysis of fMRI data (p-value < 0.01). 26
5.8 Activation area from ΔHbO_2 using (a) pre-whitening, fOSA, (b) pre-coloring, fOSA, (c) pre-whitening, incomplete gamma bound, (d) pre-coloring, incomplete gamma bound, (e) pre-whitening, tube formula, and (f) pre-coloring, tube formula. 27
5.9 Activation area from ΔHbR using (a) pre-whitening, fOSA, (b) pre-coloring, fOSA, (c) pre-whitening, incomplete gamma bound, (d) pre-coloring, incomplete gamma bound, (e) pre-whitening, tube formula, and (f) pre-coloring, tube formula. 28

5.10 Activation area from both ΔHbO_2 and ΔHbR using (a) pre-whitening, fOSA, (b) pre-coloring, fOSA, (c) pre-whitening, incomplete gamma bound, (d) pre-coloring, incomplete gamma bound, (e) pre-whitening, tube formula, and (f) pre-coloring, tube formula. 29
5.11 T-statistic maps from ΔHbO_2 using (a) pre-whitening, fOSA, (b) pre-coloring, fOSA, (c) pre-whitening, NIRS-SPM, and (d) pre-coloring, NIRS-SPM. . . . 30
5.12 T-statistic maps from ΔHbR using (a) pre-whitening, fOSA, (b) pre-coloring, fOSA, (c) pre-whitening, NIRS-SPM, and (d) pre-coloring, NIRS-SPM. . . . 31
5.13 T-statistic maps from both ΔHbO_2 and ΔHbR using (a) pre-whitening, fOSA, (b) pre-coloring, fOSA, (c) pre-whitening, NIRS-SPM, and (d) pre-coloring, NIRS-SPM. 32
5.14 SPM analysis of fMRI data (p-value < 0.01). 33
5.15 Activation area from ΔHbO_2 using (a) pre-whitening, fOSA, (b) pre-coloring, fOSA, (c) pre-whitening, tube formula, and (d) pre-coloring, tube formula. . . 34
5.16 Activation area from ΔHbR using (a) pre-whitening, fOSA, (b) pre-coloring, fOSA, (c) pre-whitening, tube formula, and (d) pre-coloring, tube formula. . . 35
5.17 Activation area from both ΔHbO_2 and ΔRusing (a) pre-whitening, fOSA, (b) pre-coloring, fOSA, (c) pre-whitening, tube formula, and (d) pre-coloring, tube formula. 36

1. Introduction

Near infrared spectroscopy (NIRS) is a non-invasive method to measure the brain activity by measuring the absorption of the near infrared light between 650 and 950 nm through the intact skull [1]. Specifically, the absorption spectra of oxy-hemoglobin (HbO_2) and deoxy-hemoglobin (HbR) are distinct in this region, so it is possible to determine the concentration changes of oxy- and deoxy-hemoglobin from diffusely scattered light measurement [2].

NIRS has many advantages over other neuroimaging modalities such as positron emission tomography (PET), functional magnetic resonance imaging (fMRI) or magnetoencephalography (MEG). One of the main advantages is the ability to measure a wide range of functional contrast such as oxy-hemoglobin, deoxy-hemoglobin, and total hemoglobin. Furthermore, NIRS has high temporal resolution that allows us to study temporal behaviors of the hemodynamic response to neural activation and the origin of blood oxygenation level dependent signal (BOLD). Another advantage of NIRS is the high degree of flexibility in experimental use since NIRS requires only compact measurement system and is robust to the motion artifact compared to fMRI. However, NIRS is lack of the anatomical information, making it difficult to localize the brain area where the NIRS signal is originated [3]. Moreover, NIRS has poor spatial resolution and limited penetration depth due to the high level of light scattering within tissue.

Simultaneous recording with NIRS and fMRI can provide a solution to overcome these disadvantages, since MRI provides the location of optical probes with respect to underlying brain. In addition, the integration with NIRS and fMRI promises a significant mutual enhancement of temporal and spatial resolutions because optically measured hemoglobin signal strongly correlates with fMRI BOLD signal[4]. Thus, the main goal of our research is to develop an integrated system for simultaneously recording and statistically analyzing the NIRS and fMRI.

Recently, many researchers have been developing statistical analysis toolbox for NIRS based on generalized linear model (GLM) [5, 6, 7]. GLM is a statistical linear model that explains data as a linear combination of an explanatory variable plus an error term. Because GLM measures the temporal variational pattern of signals rather than their absolute magnitude, GLM is robust to many cases even with a severe optical signal attenuation due to scattering or poor contact. Since this statistical parameter mapping (SPM) using GLM has become the standard method for analyzing the fMRI data [8], an integration of NIRS

and fMRI within the same SPM framework has an advantage with modeling both types of data in the same mathematical framework to make the classical inference.

Recently, Koh et al [7] have developed an extensive statistical NIRS analysis tools called functional optical signal analysis (fOSA), which applies the SPM method to NIRS data. They showed that most of the SPM framework can be successfully applied to NIRS data with slight modification. However, several fundamental issues still remain unsolved. For example, even though Gaussian random field theory has been used and justified in fOSA as a tool for inference, the basic assumption for Gaussian random field model breaks down in NIRS. Recall that SPM for fMRI analysis assumes that the residuals after the GLM fitting are *dense* samples on lattice representations from an underlying continuous Gaussian random field [9] due to the Gaussian kernel smoothing. However, because the distance between each channel of NIRS is far and the number of measurements are sparse, it is not reasonable to use Gaussian random field theory in making inference of NIRS data. Furthermore, the resolution of fOSA is limited by the distance between the optode, which makes it difficult to co-registrate with fMRI activation map.

The main contribution of this article is a new theory for statistical inference and the corresponding public domain software called NIRS-SPM. While the SPM for fMRI calculates the excursion probability of *homogenous* Gaussian random field by *smoothing* samples on *dense* lattice, NIRS requires the excursion probability of *inhomogenous* Gaussian random field obtained by *interpolating* samples on *sparsely* and *irregularly* distributed optode locations. Even though excursion probability for inhomogeneous random field is extremely difficult to calculate in general, the excursion probability for strikingly similar inhomogeneous random field model has been studied for the so-called global confidence region analysis of 3-D parametric shape estimation problem [10] using Sun's tube formula [11]. For example, the p-value for the one side t- test for oxy- or deoxy-hemoglobin concentration can be converted into the excursion probability of Gaussian random field on a two dimensional *representation manifold* that is dependent on the structure of covariance matrix and the interpolating kernels. Furthermore, we can extend the result to calculate p-value of the simultaneous activation of oxy- and deoxy- hemoglobin signals by calculating an excursion probability of Gaussian random field on a three dimensional representation manifold. Thanks to these powerful tools for excursion probability, NIRS-SPM enables super-resolution localization of the brain activation, which was not possible using any other conventional methods such as fOSA.

This paper also describes several other techniques to optimize our NIRS-SPM. First, in estimating the temporal correlations, we compare the pre-coloring and pre-whitening

methods introduced in fMRI model [12]. Even though the pre-whitening method is the most efficient approach to parameter estimation and currently implemented in SPM, the difference between the assumed and the actual correlations can produce some bias that make profound effects in inference. Hence, the appropriate method for estimating the temporal correlations in NIRS data is proposed. Second, in order to localize the NIRS signal to the cerebral cortex of anatomical T1 image which is obtained from MRI, Horn's algorithm [13] is implemented in NIRS-SPM. Finding the relationship between the real 3-D space and the MR image domain using pairs of coordinates in both systems is a well known problem called as absolute orientation. A closed-form, least-square solution for this problem is implemented as described in Horn (1987) [13].

This paper is organized as follows. Section 2 provides a brief review of SPM for fMRI model. In Section 3 and Section 4, an optimized framework of SPM appropriate to NIRS is described in detail. Experimental results about finger tapping and working memory task are presented in Section 5. Conclusions are presented in Section 6.

KAIST

2. A Brief Review of SPM

Statistical parametric mapping (SPM) is a continuous statistical process for localizing differences in the regional cerebral activity [14]. SPM mainly consists of two parts: general linear model and Gaussian random field theory. Since changes in oxy- or deoxy-hemoglobin concentration has strong correlation with BOLD signal [4], we will briefly review each part of SPM with respect to fMRI model. For more detailed description, see [12].

2.1 General Linear Model

GLM describes a i-th voxel measurement $\mathbf{y}^{(i)} \in \mathbb{R}^N$ in terms of a linear combination of explanatory variables plus an error term:

$$\mathbf{y}^{(i)} = \mathbf{X}\boldsymbol{\beta}^{(i)} + \boldsymbol{\epsilon}^{(i)}, \tag{2.1}$$

where $\mathbf{X} \in \mathbb{R}^{N \times M}$ is the design matrix composed of M covariates, and $\boldsymbol{\beta}^{(i)} \in \mathbb{R}^M$ is unknown strength of response. The error $\boldsymbol{\epsilon}^{(i)} \in \mathbb{R}^M$ is assumed to be normally distributed with zero mean but possibly temporally correlated.

Assuming that BOLD signal is the output of a linear time-invariant system [16], each column of design matrix, which is the predicted hemodynamic response in specific experimental condition, can be expressed as a convolution of a stimulus function with a hemodynamic response function (HRF). Since the precise shape of the HRF varies across the brain, the two derivatives of HRF with respect to delay and dispersion have been used to mitigate that problem [15].

After specifying the design matrix, the relative contribution of each element of these columns, $\hat{\boldsymbol{\beta}}$, is estimated using ordinary least square. If the design matrix is of full rank, the least square estimates is given as following:

$$\hat{\boldsymbol{\beta}}^{(i)} = \mathbf{X}^{\dagger}\mathbf{y}^{(i)}, \tag{2.2}$$

where $\mathbf{X}^{\dagger} = (\mathbf{X}^T\mathbf{X})^{-1}\mathbf{X}^T$ denotes the pseudo-inverse. When forming t- or F- statistics, the temporal correlation structure should be investigated in order to obtain the unbiased estimate of standard error. In estimation of error covariance matrix, SPM assumes that temporal correlation matrix is the same at all voxels, however variance is different. Hence,

the error covariance matrix at the i-th voxel is given by:

$$\mathbf{C}_{\boldsymbol{\epsilon}^{(i)}} = E\left[\boldsymbol{\epsilon}^{(i)}\boldsymbol{\epsilon}^{(i)T}\right] = \left(\sigma^{(i)}\right)^2 \boldsymbol{\Lambda} \tag{2.3}$$

where $\boldsymbol{\Lambda}$ is the temporal correlation matrix and $\left(\sigma^{(i)}\right)^2$ denotes the variance, respectively.

Usually, the autoregressive (order 1) plus white noise model (AR(1) + wn) [17] is used for investigating the temporal correlations in fMRI data. Due to the stability issue, the actual implementation of SPM for AR model is realized by linear approximation with basis set defined as following:

$$\boldsymbol{\Lambda} = \sum_{l=1}^{2} \lambda_l \mathbf{Q}_l, \tag{2.4}$$

with

$$\mathbf{Q}_1 = \mathbf{I}_N, \quad [\mathbf{Q}_2]_{ij} = \begin{cases} e^{-|i-j|}, & i \neq j \\ 0, & i = j, \end{cases} \tag{2.5}$$

where λ_l are the hyperparameters and $\mathbf{Q}_1$, $\mathbf{Q}_2$ are default basis set for temporal correlation in fMRI data. These hyperparameters are then estimated by using iterative restricted maximum likelihood (ReML) algorithm [18]. Then, variance $\sigma^{(i)2}$ at each voxel can be estimated using the usual estimator in a least squares mass-univariate scheme:

$$\left(\sigma^{(i)}\right)^2 = \frac{\mathbf{y}^{(i)T}\mathbf{R}\mathbf{y}^{(i)}}{trace\left(\mathbf{R}\boldsymbol{\Lambda}\right)}, \tag{2.6}$$

with the residual forming matrix $\mathbf{R} = \mathbf{I} - \mathbf{X}\left(\mathbf{X}^T\mathbf{X}\right)^{-1}\mathbf{X}^T$ [8].

Inference about the particular linear combination of estimate $\hat{\boldsymbol{\beta}}^{(i)}$ can be obtained using t-statistics. Because the error $\epsilon^{(i)}$ is normally distributed with $\epsilon \sim \mathcal{N}\left(\mathbf{O}, \sigma^{(i)2}\boldsymbol{\Lambda}\right)$, under the null hypothesis the estimate $\hat{\boldsymbol{\beta}}^{(i)}$ which is weighted with contrast vector $\mathbf{c}$ also has normal distribution as following:

$$\mathbf{c}^T\hat{\boldsymbol{\beta}}^{(i)} \sim \mathcal{N}(0, \sigma^{(i)2}\mathbf{c}^T\mathbf{X}^{\dagger}\boldsymbol{\Lambda}\mathbf{X}^{\dagger T}\mathbf{c}). \tag{2.7}$$

Thus, a contrast t-statistic against null hypothesis can be obtained as following:

$$T^{(i)} = \frac{\mathbf{c}^T\hat{\boldsymbol{\beta}}^{(i)}}{\sqrt{\hat{\sigma^{(i)}}^2\mathbf{c}^T\mathbf{X}^{\dagger}\boldsymbol{\Lambda}\mathbf{X}^{\dagger T}\mathbf{c}}}, \tag{2.8}$$

where the effective degrees of freedom are given by:

$$df = \frac{trace(\mathbf{R}\boldsymbol{\Lambda})^2}{trace(\mathbf{R}\boldsymbol{\Lambda}\mathbf{R}\boldsymbol{\Lambda})}. \tag{2.9}$$

2.2 Gaussian Random Field Theory

Let the random field $Z(r), r \in \Psi$ denote the $t-$ statistics. One of the methods to select an activated region among the random field $Z(r)$ is to threshold the statistic value Z at the height z. Then, the most important quantity for this type of analysis is to calculate the p-value of such activation map. More specifically, the p-value of our interest is given by the excursion probability of the continuous random field:

$$p = P\left\{\max_{r\in\Psi} Z(r) > z\right\} \tag{2.10}$$

The Bonferroni correction is a basic method to choose the threshold in multiple comparisons as following:

$$P\left\{\max_{r\in\Psi} Z(r) > z\right\} \geq 1 - \left(P\left\{Z(r_i) < z\right\}\right)^N, \tag{2.11}$$

where $\{r_i\}_{i=1}^N$ denotes the lattice coordinates on Ψ. Because Eq. (2.11) is derived for independent random variables, Bonferroni correction is not appropriate to the functional imaging data that are spatially correlated.

In case of smooth statistical maps, random field theory is typically used for adjusting p-value as following [12]:

KAIST

$$P(\max_{r\in\Psi} Z(r) > z) \approx \sum_{d=0}^{D} Resels_d \cdot EC_d(z), \tag{2.12}$$

where D is the number of dimensions of the search region, $Resels_d$ is the number of d-dimensional resels (resolution elements) in the search region, and $EC_d(z)$ is the d-dimensional Euler characteristic [19]. However, in order to use Eq. (2.12), it is necessary to satisfy the following two assumptions: 1. The error fields are a reasonable lattice approximation to an underlying random field with a multivariate Gaussian distribution. 2. These fields are continuous, with a differentiable and invertible autocorrelation function. This requires that the voxel size is relatively smaller than the smoothness with an isotropic Gaussian kernel. [9, 12]. However, because the NIRS has inherently poor spatial resolution and the optode distances are very far compared to the fMRI, it is not reasonable to use Gaussian random field theory in making inference of NIRS data.

3. Statistical Parametric Mapping for Near Infrared Spectroscopy

3.1 Measurement Model for NIRS

The modified Beer-Lambert law (MBLL) which describes an optical attenuation in a highly scattering medium like biological tissue [20] allows the transformation from raw optical density (OD) data to changes of chromophore concentrations. According to the MBLL, the change in $OD(\lambda, r, t)$ at the wavelength λ from the cerebral cortex position r at time t due to the N_c number of chromophore concentration changes $\{\Delta c^{(i)}(r,t)\}_{i=1}^{N_c}$ is described as

$$\triangle OD(\lambda, r, t) = -ln\left(\frac{I_F}{I_o}\right) = \sum_{i=1}^{N_c} a_i(\lambda) \triangle c^{(i)}(r,t) d(r) l(r) \tag{3.1}$$

where I_F denote the final measured optical intensity, I_o denotes the initial measured optical intensity, $a_i(\lambda)$ is the extinction coefficient of the i-th chromophore at the wavelength λ, $d(r)$ is the differential pathlength factor (DPF), and $l(r)$ is the distance between the source and detector at the position r, respectively. Assuming that oxy- and deoxy- hemoglobin are the major two choromophores, the noisy measured optical density is then described with the matrix formulation as follow:

$$\begin{bmatrix} \Delta OD(r,t;\lambda_1) \\ \Delta OD(r,t;\lambda_2) \end{bmatrix} = d(r)l(r) \begin{bmatrix} a_1(\lambda_1) & a_2(\lambda_1) \\ a_1(\lambda_2) & a_2(\lambda_2) \end{bmatrix} \begin{bmatrix} \Delta c_{HbO_2}(r,t) \\ \Delta c_{HbR}(r,t) \end{bmatrix} + \begin{bmatrix} w(r,t;\lambda_1) \\ w(r,t;\lambda_2) \end{bmatrix} \tag{3.2}$$

where $\Delta c_{HbO_2}(r,t), \Delta c_{HbR}(r,t)$ denote the time-series of the chromophore changes for the oxy- and deoxy-hemoglobin; and $w(r,t;\lambda_1), w(r,t;\lambda_2)$ are the additive noise at the wavelength λ_1 and λ_2, respectively. Then, by multiplying the inverse matrix of the extinction coefficients with Eq. (3.2), we have the noisy measurement of oxy- and deoxy- hemoglobin concentration changes:

$$\begin{bmatrix} y_{HbO_2}(r,t) \\ y_{HbR}(r,t) \end{bmatrix} = d(r)l(r) \begin{bmatrix} \Delta c_{HbO_2}(r,t) \\ \Delta c_{HbR}(r,t) \end{bmatrix} + \begin{bmatrix} \epsilon_{HbO_2}(r,t) \\ \epsilon_{HbR}(r,t) \end{bmatrix} \tag{3.3}$$

where $\epsilon_{HbO_2}(r,t)$ and $\epsilon_{HbR}(r,t)$ are additive zero mean Gaussian noise for oxy- and deoxy-channel. In practice, it is impossible to measure the exact value of $d(r)$ and $l(r)$. This

is because that the NIRS data acquisition is considerably affected by variety of measurement conditions such as the color of hair and the scalp depth, which make the position- and subject- dependent scattering effect. Non-uniform contact between optodes and a scalp might be another source of the variation of sensitivities of detectors. There are other experimental issues such as the subject's movement during the experiment. For these reasons, analyzing NIRS data with the absolute value of chromophore concentration is problematic.

3.2 General Linear Model for NIRS

In this section, we will show that GLM approach enables an accurate analysis for NIRS. Even though we mainly focus on the GLM for the oxy- hemoglobin concentration, exactly same approach can be applied for deoxy- hemoglobin concentration.

Let $\mathbf{y}_{HbO_2}^{(i)} \in \mathbb{R}^N$ and $\boldsymbol{\epsilon}_{HbO_2}^{(i)} \in \mathbb{R}^N$ denote the time series of the oxy- hemoglobin signal and noise at the i-th channel at the location r_i:

$$\mathbf{y}_{HbO_2}^{(i)} = \begin{bmatrix} y_{HbO_2}(r_i,t_1) & y_{HbO_2}(r_i,t_2) & \cdots & y_{HbO_2}(r_i,t_N) \end{bmatrix}^T, \tag{3.4}$$

$$\boldsymbol{\epsilon}_{HbO_2}^{(i)} = \begin{bmatrix} \epsilon_{HbO_2}(r_i,t_1) & \epsilon_{HbO_2}(r_i,t_2) & \cdots & \epsilon_{HbO_2}(r_i,t_N) \end{bmatrix}^T. \tag{3.5}$$

Then, corresponding GLM model is given by

$$\mathbf{y}_{HbO_2}^{(i)} = \mathbf{X}_{HbO_2}\boldsymbol{\beta}_{HbO_2}^{(i)} + \boldsymbol{\epsilon}_{HbO_2}^{(i)} \tag{3.6}$$

where $\mathbf{X}_{HbO_2} \in \mathbb{R}^{N\times M}$ denotes the design matrices for oxy- hemoglobin, and $\boldsymbol{\beta}_{HbO_2}^{(i)} \in \mathbb{R}^M$ is the corresponding response signal strength at the i-th channel, respectively. By stacking the measurements from all K channels, we have

$$\begin{aligned} \mathbf{y}_{HbO_2} &= \begin{bmatrix} \mathbf{y}_{HbO_2}^{(1)} \\ \mathbf{y}_{HbO_2}^{(2)} \\ \vdots \\ \mathbf{y}_{HbO_2}^{(K)} \end{bmatrix} = \begin{bmatrix} \mathbf{X}_{HbO_2} & \mathbf{O} & \cdots & \mathbf{O} \\ \mathbf{O} & \mathbf{X}_{HbO_2} & \cdots & \mathbf{O} \\ \vdots & \vdots & \ddots & \vdots \\ \mathbf{O} & \mathbf{O} & \cdots & \mathbf{X}_{HbO_2} \end{bmatrix} \begin{bmatrix} \boldsymbol{\beta}_{HbO_2}^{(1)} \\ \boldsymbol{\beta}_{HbO_2}^{(2)} \\ \vdots \\ \boldsymbol{\beta}_{HbO_2}^{(K)} \end{bmatrix} + \begin{bmatrix} \boldsymbol{\epsilon}_{HbO_2}^{(1)} \\ \boldsymbol{\epsilon}_{HbO_2}^{(2)} \\ \vdots \\ \boldsymbol{\epsilon}_{HbO_2}^{(K)} \end{bmatrix} \\ &= \left(\mathbf{I}^{K\times K} \otimes \mathbf{X}_{HbO_2}\right)\boldsymbol{\beta}_{HbO_2} + \boldsymbol{\epsilon}_{HbO_2} \end{aligned} \tag{3.7}$$

where $\mathbf{I}^{K\times K}$ denotes the $K \times K$ identity matrix, $\otimes$ is the Kronecker product, and

$$\boldsymbol{\beta}_{HbO_2} = \begin{bmatrix} \boldsymbol{\beta}_{HbO_2}^{(1)} \\ \boldsymbol{\beta}_{HbO_2}^{(2)} \\ \vdots \\ \boldsymbol{\beta}_{HbO_2}^{(K)} \end{bmatrix} \in \mathbb{R}^{KM\times 1} \quad , \quad \boldsymbol{\epsilon}_{HbO_2} = \begin{bmatrix} \boldsymbol{\epsilon}_{HbO_2}^{(1)} \\ \boldsymbol{\epsilon}_{HbO_2}^{(2)} \\ \vdots \\ \boldsymbol{\epsilon}_{HbO_2}^{(K)} \end{bmatrix} \in \mathbb{R}^{KM\times 1} \tag{3.8}$$

Using the property of the Kronecker product, the least square estimation of $\boldsymbol{\beta}_{HbO_2}$ is given by

$$\hat{\boldsymbol{\beta}}_{HbO_2} = \left(\mathbf{I}^{K\times K} \otimes \mathbf{X}^{\dagger}_{HbO_2}\right) \mathbf{y}_{HbO_2} \tag{3.9}$$

where $\mathbf{X}^{\dagger}_{HbO_2} = \left(\mathbf{X}^{T}_{HbO_2}\mathbf{X}_{HbO_2}\right)^{-1}\mathbf{X}^{T}_{HbO_2}$ denotes the pseudo-inverse of $\mathbf{X}_{HbO_2}$. Under the null hypothesis, the mean value of the response signal strength is zero. Hence, the corresponding estimation error covariance matrix is given by

$$\begin{aligned} \mathbf{C}_{\hat{\boldsymbol{\beta}}_{HbO_2}} &= E\left[\hat{\boldsymbol{\beta}}_{HbO_2}\hat{\boldsymbol{\beta}}^{H}_{HbO_2}\right] \\ &= \left(\mathbf{I}^{K\times K} \otimes \mathbf{X}^{\dagger}_{HbO_2}\right) \mathbf{C}_{\boldsymbol{\epsilon}_{HbO_2}} \left(\mathbf{I}^{K\times K} \otimes \mathbf{X}^{\dagger T}_{HbO_2}\right) \end{aligned} \tag{3.10}$$

Since each channel in NIRS measurement is located in relative far distances, we can safely assume that the noises from different channels are linear independent. Using our covariance model Eq. (2.3), we then have

$$\mathbf{C}_{\boldsymbol{\epsilon}_{HbO_2}} = \begin{bmatrix} \sigma^{(1)2}_{HbO_2}\boldsymbol{\Lambda}_{HbO_2} & \mathbf{O} & \cdots & \mathbf{O} \\ \mathbf{O} & \sigma^{(2)2}_{HbO_2}\boldsymbol{\Lambda}_{HbO_2} & \cdots & \mathbf{O} \\ \vdots & \vdots & \ddots & \vdots \\ \mathbf{O} & \mathbf{O} & \cdots & \sigma^{(K)2}_{HbO_2}\boldsymbol{\Lambda}_{HbO_2} \end{bmatrix} = \boldsymbol{\Sigma}_{HbO_2} \otimes \boldsymbol{\Lambda}_{HbO_2} \tag{3.11}$$

where

$$\boldsymbol{\Sigma}_{HbO_2} = \begin{bmatrix} \sigma^{(1)2}_{HbO_2} & \mathbf{O} & \cdots & \mathbf{O} \\ \mathbf{O} & \sigma^{(2)2}_{HbO_2} & \cdots & \mathbf{O} \\ \vdots & \vdots & \ddots & \vdots \\ \mathbf{O} & \mathbf{O} & \cdots & \sigma^{(K)2}_{HbO_2} \end{bmatrix} \tag{3.12}$$

Finally, the properties of Kronecker product lead us:

$$\begin{aligned} \mathbf{C}_{\hat{\boldsymbol{\beta}}_{HbO_2}} &= \left(\mathbf{I}^{K\times K} \otimes \mathbf{X}^{\dagger}_{HbO_2}\right) \left(\boldsymbol{\Sigma}_{HbO_2} \otimes \boldsymbol{\Lambda}_{HbO_2}\right) \left(\mathbf{I}^{K\times K} \otimes \mathbf{X}^{\dagger T}_{HbO_2}\right) \\ &= \left(\boldsymbol{\Sigma}_{HbO_2} \otimes \mathbf{X}^{\dagger}_{HbO_2}\boldsymbol{\Lambda}_{HbO_2}\mathbf{X}^{\dagger T}_{HbO_2}\right) \end{aligned} \tag{3.13}$$

The main difficulty in analyzing NIRS is that there exists only small number of optodes and the distance between the optodes is relatively large; hence, direct application of Gaussian random field model for inference is not appropriate for NIRS. Furthermore, in order to study the correlation with fMRI, it is preferable that the NIRS data should be interpolated to the same resolution as fMRI. Specifically, the interpolated response signal strength at $r \in \Psi$ is given as follows:

$$\hat{\boldsymbol{\alpha}}_{HbO_2}(r) = \sum_{i=1}^{K} \boldsymbol{\beta}^{(i)}_{HbO_2} b_i(r) = \left(\mathbf{b}(r)^T \otimes \mathbf{I}^{M\times M}\right) \hat{\boldsymbol{\beta}}_{HbO_2} \in \mathbb{R}^M \tag{3.14}$$

where $\mathbf{b}(r)$ denotes the interpolating kernel given by

$$\mathbf{b}(r) = \begin{bmatrix} b_1(r) & b_2(r) & \cdots & b_K(r) \end{bmatrix}^T \in \mathbb{R}^{K \times 1} \tag{3.15}$$

Usually, the response of the signal we are interested in are calculated by inner product with a contrast vector:

$$\begin{aligned} X_{HbO_2}(r) &= \mathbf{c}^T \hat{\boldsymbol{\alpha}}_{HbO_2}(r) \\ &= \mathbf{c}^T \left(\mathbf{b}(r)^T \otimes \mathbf{I}^{M \times M} \right) \hat{\boldsymbol{\beta}}_{HbO_2} = \mathbf{B}(r)^T \hat{\boldsymbol{\beta}}_{HbO_2} \end{aligned} \tag{3.16}$$

The corresponding error variance is

$$\begin{aligned} C_{X,HbO_2}(r) &= \mathbf{B}(r)^T \mathbf{C}_{\hat{\boldsymbol{\beta}},HbO_2} \mathbf{B}(r) \\ &= \mathbf{c}^T \left(\mathbf{b}(r)^T \otimes \mathbf{I}^{M \times M} \right) \left(\boldsymbol{\Sigma}_{HbO_2} \otimes \mathbf{X}^{\dagger}_{HbO_2} \boldsymbol{\Lambda}_{HbO_2} \mathbf{X}^{\dagger T}_{HbO_2} \right) \left(\mathbf{b}(r) \otimes \mathbf{I}^{M \times M} \right) \mathbf{c} \\ &= \left(\mathbf{b}(r)^T \boldsymbol{\Sigma}_{HbO_2} \mathbf{b}(r) \right) \left(\mathbf{c}^T \mathbf{X}^{\dagger}_{HbO_2} \boldsymbol{\Lambda}_{HbO_2} \mathbf{X}^{\dagger T}_{HbO_2} \mathbf{c} \right) \end{aligned} \tag{3.17}$$

Now, under the null hypothesis the response signal $X_{HbO_2}(r)$ is distributed as zero mean Gaussian distribution:

$$X_{HbO_2}(r) \sim \mathcal{N}\left(0, C_{X,HbO_2}(r)\right) \tag{3.18}$$

KAIST

Hence, the corresponding t- statistics is given by

$$\begin{aligned} T_{HbO_2}(r) &= \frac{X_{HbO_2}(r)}{\sqrt{C_{X,HbO_2}(r)}} \\ &= \frac{\mathbf{c}^T \hat{\boldsymbol{\alpha}}_{HbO_2}(r)}{\sqrt{\left(\mathbf{b}(r)^T \boldsymbol{\Sigma}_{HbO_2} \mathbf{b}(r) \right) \left(\mathbf{c}^T \mathbf{X}^{\dagger}_{HbO_2} \boldsymbol{\Lambda}_{HbO_2} \mathbf{X}^{\dagger T}_{HbO_2} \mathbf{c} \right)}} \end{aligned} \tag{3.19}$$

3.3 Inference using Global Confidence Region Analysis

Assuming that the interpolating kernel can fully describe the baseline signal between the optode locations, our goal is to calculate the p-value where the null hypothesis can be abandoned. This can be calculated as an excursion probability of the resultant random field. More specifically, we are interested in calculating the following exceedence probabilities:

- One side t- test for HbO_2: $P\left\{\max_{r \in \Psi} T_{HbO_2}(r) \geq z\right\}$.
- One side t- test for HbR: $P\left\{\max_{r \in \Psi} T_{HbR}(r) \geq z\right\}$.

- Two side t- test for both HbO_2 and HbR: $P\left\{\max_{r\in\Psi}\left(T_{HbO_2}(r)\right)^2+\left(T_{HbR}(r)\right)^2\geq z^2\right\}$

While the form of exceedence probability appears similar to that of the excursion probability of Gaussian random field in SPM for fMRI, there exist fundamental differences. Note that the Gaussian random field in fMRI comes from the Gaussian kernel *smoothing* of discrete signals on a *dense* lattice, whereas our exceedence probability comes from the random field that is *interpolated* from *sparse* measurement (Figs. 3.1). Therefore, we cannot use the p-value taylored for the Gaussian random field in the conventional SPM.

Interestingly, similar exceedence probability has been extensively studied for the so-called global confidence region analysis for 3-D parametric shape estimation problem [10]. They showed that the resultant random field is *inhomogeneous* and its excursion statistics can be calculated using Sun's tube formula [11]. Hence, we follow the approach in [10] and calculate the p-values.

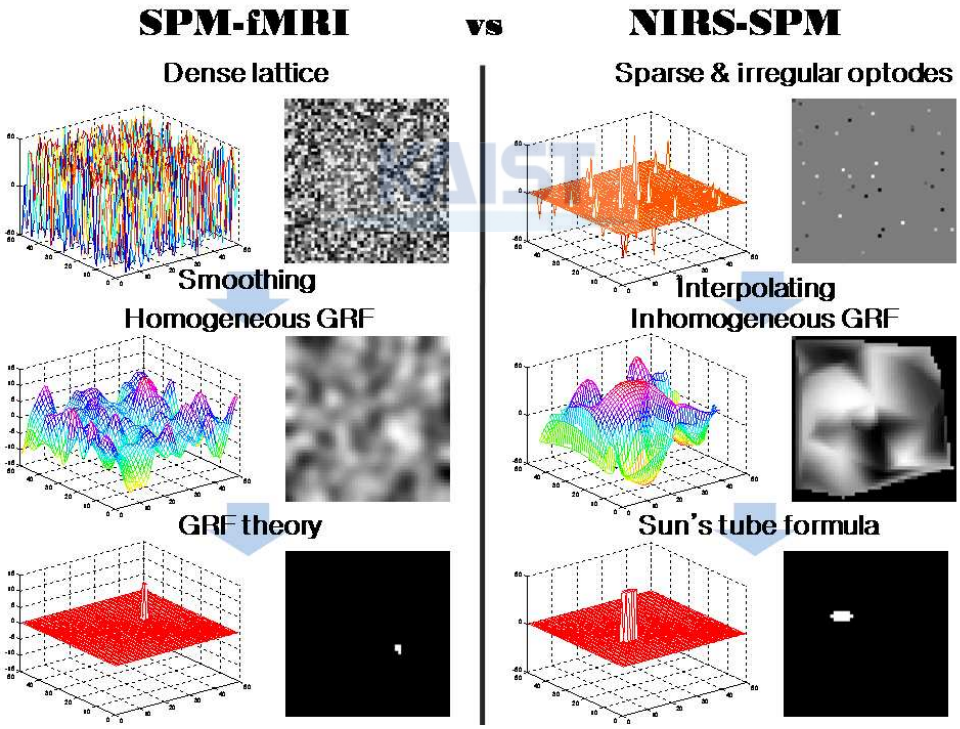

Figure 3.1: The difference between fMRI and NIRS model.

3.3.1 One-side t-test for HbO_2 or HbR

In this section, all the derivation will be done for HbO_2. However, the formula for p-value for the case of HbR can be derived in a same manner. Note that the p-value of the t- statistics to abandon null hypothesis is given by:

$$p = P\left\{\max_{r\in\Psi} T_{HbO_2}(r) \geq z\right\} = \frac{1}{2}P\left\{\max_{r\in\Psi} |T_{HbO_2}(r)|^2 \geq z^2\right\} \tag{3.20}$$

due to the symmetry of the $T_{HbO_2}(r)$ around zero. Now, we have

$$\begin{aligned} P\left\{\max_{r\in\Psi} |T_{HbO_2}(r)|^2 \geq z^2\right\} &= P\left\{\max_{r\in\Psi} \boldsymbol{\alpha}_{HbO_2}^T(r) C_{X,HbO_2}(r)^{-1} \boldsymbol{\alpha}_{HbO_2}(r) \geq z^2\right\} \\ &= P\left\{\max_{r\in\Psi} \hat{\boldsymbol{\beta}}_{HbO_2}^T \mathbf{B}(r)\Big(\mathbf{B}(r)^T \mathbf{C}_{\hat{\boldsymbol{\beta}},HbO_2} \mathbf{B}(r)\Big)^{-1} \mathbf{B}(r)^T \hat{\boldsymbol{\beta}}_{HbO_2} \geq z^2\right\} \\ &= P\left\{\max_{r\in\Psi} \mathbf{Z}^T \mathbf{C}_{\hat{\boldsymbol{\beta}},HbO_2}^{1/2} \mathbf{B}(r)\Big(\mathbf{B}(r)^T \mathbf{C}_{\hat{\boldsymbol{\beta}},HbO_2} \mathbf{B}(r)\Big)^{-1} \mathbf{B}(r)^T \mathbf{C}_{\hat{\boldsymbol{\beta}},HbO_2}^{1/2} \mathbf{Z} \geq z^2\right\} \\ &= P\left\{\max_{r\in\Psi} \mathbf{Z}^T \mathbf{P}_{HbO_2}(r) \mathbf{Z} \geq z^2\right\} \end{aligned} \tag{3.21}$$

with

$$\mathbf{Z} \triangleq \mathbf{C}_{\hat{\boldsymbol{\beta}},HbO_2}^{-1/2} \boldsymbol{\beta}_{HbO_2} \in \mathbb{R}^{KM} \tag{3.22}$$

$$\mathbf{P}_{HbO_2}(r) \triangleq \mathbf{C}_{\hat{\boldsymbol{\beta}},HbO_2}^{1/2} \mathbf{B}(r) \left(\mathbf{B}^T(r) \mathbf{C}_{\hat{\boldsymbol{\beta}},HbO_2} \mathbf{B}(r)\right)^{-1} \mathbf{B}^T(r) \mathbf{C}_{\hat{\boldsymbol{\beta}},HbO_2}^{1/2} \tag{3.23}$$

where $\mathbf{Z} \sim \mathcal{N}\left(\mathbf{O}, \mathbf{I}^{KM\times KM}\right)$ denotes the zero-mean independent Gaussian random vector and $\mathbf{P}_{HbO_2}(r)$ is the $KM \times KM$ projection matrix onto the range space of $\mathbf{C}_{\hat{\boldsymbol{\beta}},HbO_2}^{1/2} \mathbf{B}(r)$, which is well defined for all $r \in \Psi$. Using Eqs. (3.16) and (3.17), we have

$$\mathbf{P}_{HbO_2}(r) = \mathbf{u}_{HbO_2}(r) \mathbf{u}_{HbO_2}(r)^T \tag{3.24}$$

where the unit vector $\mathbf{u}_{HbO_2}$ is given by

$$\mathbf{u}_{HbO_2} = \frac{\mathbf{C}_{\hat{\boldsymbol{\beta}},HbO_2}^{1/2} \left(\mathbf{b}(r) \otimes \mathbf{I}^{M\times M}\right) \mathbf{c}}{\sqrt{\mathbf{b}(r)^T \boldsymbol{\Sigma}_{HbO_2} \mathbf{b}(r)} \sqrt{\mathbf{c}^T \mathbf{X}_{HbO_2}^{\dagger} \boldsymbol{\Lambda}_{HbO_2} \mathbf{X}_{HbO_2}^{\dagger T} \mathbf{c}}} \tag{3.25}$$

Ye et al.(2006)[10] derived the two approximation for the probability in Eq. (3.39). First, the incomplete gamma bound comes as following:

$$P\left\{\max_{r\in\Psi} \mathbf{Z}^T \mathbf{P}_{HbO_2}(r) \mathbf{Z} \geq z^2\right\} \geq P\left\{\max_{r\in\Psi} \mathbf{Z}^T \mathbf{Z} \geq z^2\right\} = 1 - \Gamma\left(\frac{KM}{2}, \frac{z^2}{2}\right). \tag{3.26}$$

For small number of channels (i.e. K is smaller), incomplete gamma bound is quite tight [10]. However, for large number of channels, we may need more accurate approximation.

This can be calculated using Sun's tube formula [11]. Now, let us define an inhomogeneous Gaussian random field

$$X_{HbO_2}(r) = \mathbf{u}_{HbO_2}(r)^H \mathbf{Z} \tag{3.27}$$

Note that its covariance matrix can be simply represented as:

$$\mathbf{C}_X(r, r') = \sum_{i=1}^{KM} u_i(r) u_i(r') \tag{3.28}$$

where $u_i(r)$ denotes the i-th elements of $\mathbf{u}(r)$. Since the Gaussian random field $X_{HbO_2}(r)$ is completely determined by its covariance function $\mathbf{C}_X(r, r')$, a more compact representation for $X(r)$ is in terms of the two-dimensional *representation manifold* [10]:

$$\mathcal{U} \triangleq \{\mathbf{u}_{HbO_2}(r), r \in \Psi\} \quad \subset \mathbb{R}^{KM}. \tag{3.29}$$

While the functional representation $\mathbf{u}(\cdot)$ of a manifold is nonunique, there are several quantities that are intrinsically related $\mathcal{U}$. One of them is the 2×2 *metric tensor matrix*:

$$\mathbf{R}(r) \triangleq E[\nabla X_{HbO_2}(r) \nabla^T X_{HbO_2}(r)] \tag{3.30}$$

Then, finally we derive the following approximation:

$$P\left\{\max_{r \in \Psi} \mathbf{Z}^T \mathbf{P}_{HbO_2}(r) \mathbf{Z} \geq z^2\right\} \simeq \kappa_0 \psi_0(z) \tag{3.31}$$

where

$$\kappa_0 = |\mathcal{U}| = \int_\Psi \sqrt{|\det(\mathbf{R}(r))|} dr \tag{3.32}$$

and

$$\psi_0(z) = \frac{\Gamma\left(\frac{3}{2}\right)}{2\pi^{3/2}} \left(1 - \Gamma\left(\frac{3}{2}, \frac{z^2}{2}\right)\right) \tag{3.33}$$

We now summarize the results in the following:

Theorem 3.1 *The p-value for the one side t- test for* $\mathrm{HbO_2}$/HbR *is lower bounded by*

$$p \quad \geq \quad \frac{1}{2}\left(1 - \Gamma\left(\frac{KM}{2}, \frac{z^2}{2}\right)\right) \tag{3.34}$$

and can be approximated as

$$p \quad \simeq \quad \frac{\kappa_0 \Gamma\left(\frac{3}{2}\right)}{4\pi^{3/2}} \left(1 - \Gamma\left(\frac{3}{2}, \frac{z^2}{2}\right)\right) \tag{3.35}$$

where κ *is given by Eq.* (3.43).

3.3.2 Two side t-test for both HbO_2 and HbR

Note that the p-value of the two side t- statistics to abandon the null hypothesis is given by:

$$P\left\{\max_{r\in\Psi}|T_{HbO_2}(r)|^2+|T_{HbR}(r)|^2\geq z^2\right\} \quad = \quad P\left\{\max_{r\in\Psi}\mathbf{Z}^T\mathbf{P}(r)\mathbf{Z}\geq z^2\right\} \tag{3.36}$$

where $\mathbf{Z}\sim\mathcal{N}\left(\mathbf{O},\mathbf{I}^{2KM\times 2KM}\right)$ denotes the zero-mean independent Gaussian random vector and

$$\mathbf{P}(r) \quad = \quad \begin{bmatrix}\mathbf{P}_{HbO_2}(r) & \mathbf{O}\\ \mathbf{O} & \mathbf{P}_{HbR}(r)\end{bmatrix}=\mathbf{U}\mathbf{U}^H \tag{3.37}$$

where rank two matrix $\mathbf{U}$ is given by

$$\mathbf{U}=\begin{bmatrix}\mathbf{u}_{HbO_2}(r) & \mathbf{O}\\ \mathbf{O} & \mathbf{u}_{HbR}(r)\end{bmatrix}\in\mathbb{R}^{2KM\times 2} \tag{3.38}$$

We again easily find the incomplete Gamma bound:

$$P\left\{\max_{r\in\Psi}|T_{HbO_2}(r)|^2+|T_{HbR}(r)|^2\geq z^2\right\} \quad \geq \quad 1-\Gamma\left(\frac{2KM}{2},\frac{z^2}{2}\right) \tag{3.39}$$

In order to use the tube formula, let us define an inhomogeneous Gaussian random field

$$X(r)=\mathbf{d}(\omega)^H\mathbf{U}(r)^H\mathbf{Z},\quad \omega\in[0,2\pi] \tag{3.40}$$

where $\mathbf{d}(\omega)=[\cos(\omega),\sin(\omega)]^T$. Note that due to the introduction of $\mathbf{d}(\omega)$, the resultant manifold becomes three dimensional:

$$\mathcal{U}=\left\{\mathbf{d}(\omega)^H\mathbf{U}(r):(\omega,r)\in[0,2\pi]\times\Psi\right\} \tag{3.41}$$

Therefore, the tube formula for the p-value is now given by

$$p \quad \simeq \quad \frac{\kappa_0\Gamma\left(\frac{4}{2}\right)}{2\pi^{4/2}}\left(1-\Gamma\left(\frac{4}{2},\frac{z^2}{2}\right)\right) \tag{3.42}$$

where κ_0 is given by

$$\kappa_0=|\mathcal{U}|=\int_0^{2\pi}d\omega\int_\Psi dr\sqrt{|\det(\mathbf{R}(\omega,r))|} \tag{3.43}$$

and

$$\mathbf{R}(\omega,r)=\begin{bmatrix}\frac{\partial\mathbf{d}(\omega)^H}{\partial\omega}\mathbf{U}(r)^H\\ \mathbf{d}(\omega)^H\frac{\partial\mathbf{U}(r)^H}{\partial r_1}\\ \mathbf{d}(\omega)^H\frac{\partial\mathbf{U}(r)^H}{\partial r_2}\end{bmatrix}\begin{bmatrix}\mathbf{U}(r)\frac{\partial\mathbf{d}(\omega)}{\partial\omega} & \frac{\partial\mathbf{U}(r)}{\partial r_1}\mathbf{d}(\omega) & \frac{\partial\mathbf{U}(r)}{\partial r_2}\mathbf{d}(\omega)\end{bmatrix}^H \tag{3.44}$$

3.4 Temporal Preprocessing: Detrending and Estimating the Temporal Correlations.

In many cases, there often exist global drifts of the NIRS measurements due to variety reasons, including subject movement during the experiment, blood pressure variation, long-term physiological changes or instrumental instability. Moreover, the amplitude of a global drift is often comparable to that of the signal from a brain activation. In order to eliminate the global trend to improve the signal-to-noise ratio, we employ the highpass filter based on a discrete cosine transform (DCT) which is currently implemented in SPM [12].

After detrending, short-range temporal correlation still exists in NIRS data. In order to obtain the correct inference in Eq.(2.8), temporal correlation structure of NIRS has to be investigated. Specifically, since the effective degrees of freedom with temporal correlation in Eq.(2.9) are lower than that of independence case, inappropriate estimate of temporal correlation causes an invalid test. To solve this problem, we compared the "pre-coloring" with "pre-whitening" methods which was proposed for fMRI model [12].

In case where temporal smoothing is strong enough to swamp any intrinsic temporal correlation, pre-coloring method is preferred. Specifically, if the full width at half maximum (FWHM) of smoothing kernel is sufficiently large, temporal correlation induced by the smoothing can be obtained without intrinsic temporal correlation:

$$\mathbf{\Lambda} = \mathbf{S\Sigma S}^T \approx \mathbf{SS}^T, \tag{3.45}$$

where $\mathbf{\Lambda}$ is a temporal correlation matrix, $\mathbf{\Sigma}$ is an intrinsic temporal correlation and $\mathbf{S}$ is a smoothing matrix which is typically derived from the canonical HRF or Gaussian smoothing kernel [21]. Because the transfer function of HRF is in the frequencies of modeled neuronal signals, we employ the canonical HRF for temporal smoothing of NIRS time-series.

An alternative way, pre-whitening, is to whiten the data using the smoothing matrix $\mathbf{S}$ which is derived from the intrinsic temporal correlation $\mathbf{\Sigma}$:

$$\mathbf{S} = \mathbf{K}^{-1}, \tag{3.46}$$

where $\mathbf{KK}^T = \mathbf{\Sigma}$ and $\mathbf{\Sigma}$ is estimated using ReML. If estimated intrinsic temporal correlation is correct, the temporal correlation structure induced by smoothing can be an identity matrix as following:

$$\mathbf{\Lambda} = \mathbf{S\Sigma S}^T = \mathbf{I} \tag{3.47}$$

In the whitened model, since the error is identically and independent distributed, least square estimate $\hat{\boldsymbol{\beta}}$ corresponds to the maximum likelihood estimate.

3.5 Spatial Preprocessing: NIRS-fMRI Alignment

In order to localize the NIRS signal with respect to the cerebral cortex of anatomical MR image, the relationship between MR coordinates and real coordinates in 3-D digitizer has to be investigated. Horn's algorithm [13] that gives a closed-form and least-square solution for this absolute orientation problem is employed.

Let $p_{MR,i}$ and $p_{NIRS,i}$ denote a measured coordinate in the MR and 3-D digitizer system, respectively, where $i = 1, 2, \ldots n$ indexes the coordinates. Let s be a scale parameter, t be a translation vector, R be a rotation matrix. Then, our problem is to find the maximum likelihood estimate for these rigid transform parameters:

$$p_{MR} = s\mathbf{R}(p_{NIRS}) + t. \tag{3.48}$$

First, all measured coordinates are redefined with respect to centroids of their systems:

$$\begin{aligned} p'_{MR,i} &= p_{MR,i} - \bar{p}_{MR}, \\ p'_{NIRS,i} &= p_{NIRS,i} - \bar{p}_{NIRS}, \\ \bar{p}_{MR} &= \frac{1}{n}\sum_{i=1}^{n} p_{MR,i}, \\ \bar{p}_{NIRS} &= \frac{1}{n}\sum_{i=1}^{n} p_{NIRS,i}. \end{aligned} \tag{3.49}$$

Then, the translation vector and the scale factor are given by

$$\begin{aligned} \hat{t} &= \bar{p}_{MR} - s\mathbf{R}(\bar{p}_{NIRS}), \\ \hat{s} &= \frac{\sum_{i=1}^{n} p'_{MR,i} \cdot R(p'_{NIRS,i})}{\sum_{i=1}^{n} \|p'_{NIRS,i}\|^2}. \end{aligned} \tag{3.50}$$

Let $p'_i = (x'_i, y'_i, z'_i)^T$ and

$$\mathbf{A}_{MR,i} = \begin{bmatrix} 0 & -x'_i & -y'_i & -z'_i \\ x'_i & 0 & -z'_i & y'_i \\ y'_i & z'_i & 0 & -x'_i \\ z'_i & -y'_i & x'_i & 0 \end{bmatrix}, \quad \mathbf{B}_{NIRS,i} = \begin{bmatrix} 0 & -x'_i & -y'_i & -z'_i \\ x'_i & 0 & z'_i & -y'_i \\ y'_i & -z'_i & 0 & x'_i \\ z'_i & y'_i & -x'_i & 0 \end{bmatrix}. \tag{3.51}$$

If we define the matrix N as

$$\mathbf{N} = \sum_{i=1}^{n} \mathbf{B}^T_{NIRS,i}\mathbf{A}_{MR,i}, \tag{3.52}$$

the vector $\hat{q}$ which is directly related to the rotation parameters is the eigenvector corresponding to the maximum eigenvalue of the matrix $\mathbf{N}$. Let $\hat{q}$ be the quaternion $(q_0, q_x, q_y, q_z)^T$

[22]. Then, the rotation matrix is obtained as following:

$$\hat{\mathbf{R}} = \begin{bmatrix} (q_0^2 + q_x^2 - q_y^2 - q_z^2) & 2(q_x q_y - q_0 q_z) & 2(q_x q_z + q_0 q_y) \\ 2(q_y q_x + q_0 q_z) & (q_0^2 - q_x^2 + q_y^2 - q_z^2) & 2(q_y q_z - q_0 q_x) \\ 2(q_z q_x - q_0 q_y) & 2(q_z q_y + q_0 q_x) & (q_0^2 - q_x^2 - q_y^2 + q_z^2) \end{bmatrix} \tag{3.53}$$

After the relationship between the MR coordinates and real coordinates in 3-D digitizer is elicited based on the measured coordinates of marker capsules, the locations of optodes in the MR coordinate can be calculated. The position of optodes are projected onto the cortical cortex which is obtained from the segmented MR images.

KAIST

4. NIRS-SPM: a New SPM Toolbox for NIRS

A new SPM appropriate to NIRS has been implemented as a "NIRS-SPM toolbox" based on SPM5 package (Wellcome Department of Cognitive Neurology, London, UK). The toolbox runs under MATLAB (Mathworks, Natick, MA), providing various computational processing from wavelet-MDL detrending to statistical analysis which is based on GLM and global confidence region based inteference (Fig. 4.1). Its statistical results are superimposed onto the 3-D rendered SPM brain map and they can be compared with fMRI result, integrating with the conventional SPM for fMRI. Figure 4.2 shows the schematic illustrating the NIRS-SPM framework.

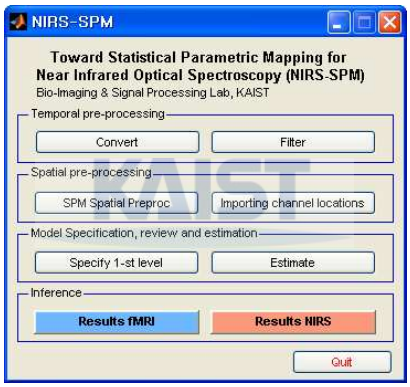

Figure 4.1: Main panel of the NIRS-SPM showing the four main groups of tools.

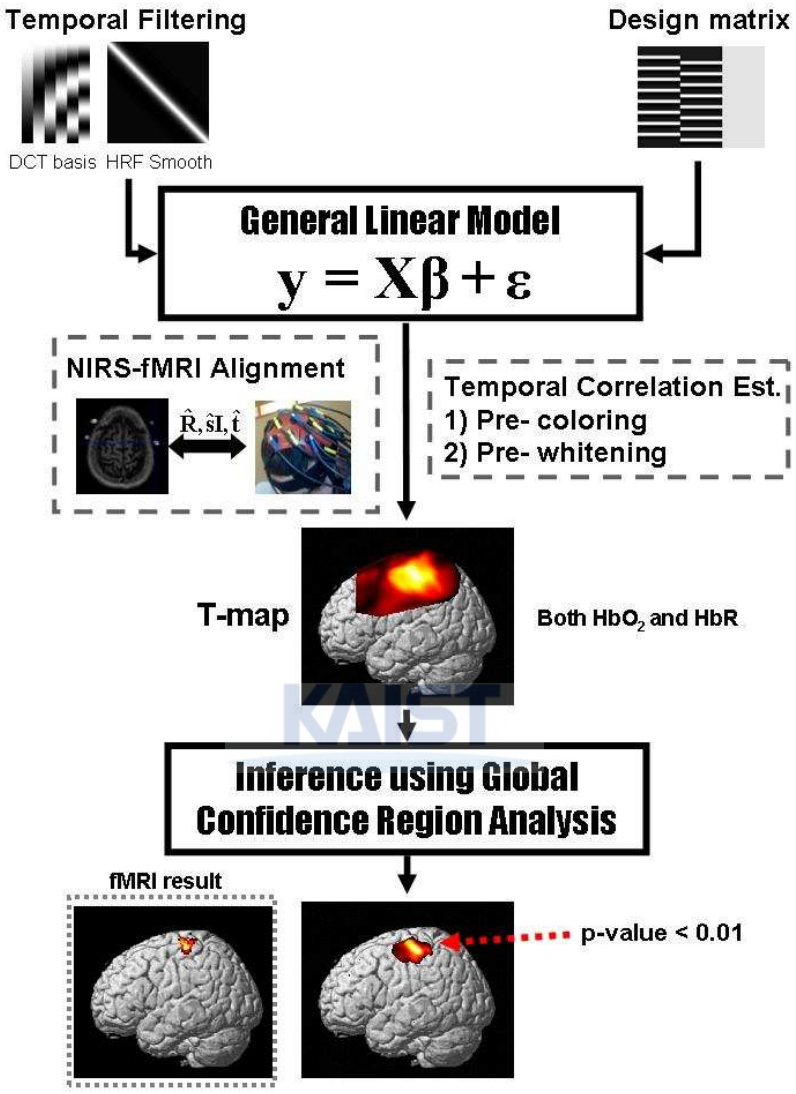

Figure 4.2: Schematic describing the NIRS-SPM framework

5. Experimental Results

5.1 Subject

All subjects were strongly right-handed. No subjects had a history of any neurological disorder. After all subjects were informed about the experimental environment as well as the operating mode of NIRS and MRI, informed consents were obtained. This study was approved by Institutional Review Board at Korea Advanced Institute of Science and Technology.

5.2 Data Acquisition

Experimental data were simultaneously acquired using NIRS and fMRI system. The NIRS system (Oxymon MK III, Artinis, Netherlands) emitted 781nm and 856nm laser lights at each source fiber. More specifically, the NIRS system has 24 channels with 8 sources and 4 detectors. Figure 5.1 shows the schematic representation of our 24 channels NIRS probe set. A holder cap to fix the distance between the source and detector optodes was attached on the scalp around left primary motor cortex and Broca's area. The distance between source and detector was 3.5 cm. The sampling rate was about 10 Hz.

MR images covering the whole brain were acquired with the echo planar imaging (EPI) sequence using a 3.0T MRI system (ISOL, Korea). Specific imaging parameters were as follows: TR/TE = 3000/35ms, flip angle = 80°, 35 slices, 4 mm slice thickness. In the subsequent anatomical scanning session, T1-weighted structural images were acquired using the same scanner.

5.3 Behavior Protocol

Each subject performed a finger tapping task and working memory task. In case of finger tapping, the 21 sec periods of activation were alternated with 30 sec periods of rest. Total recording time was 552 sec. During task period, subjects were instructed to perform a finger flexion and extension, repeatedly. In order to avoid eye and head movements, subjects were instructed to focus on the fixed point in the rest condition.

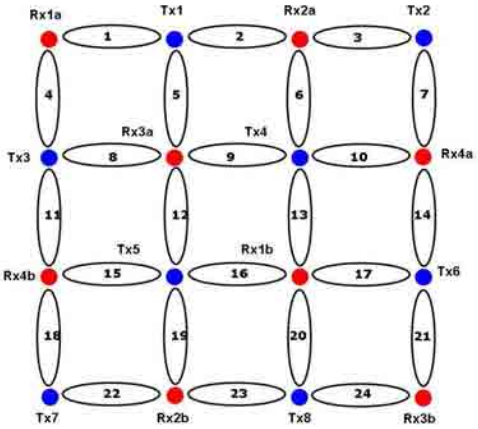

Figure 5.1: Schematic diagram of the 24 NIRS channels. Red circles are illuminators. Blue circles are detectors. Numbers between red and blue circles are NIRS channels.

The paradigm of working memory task has been designed in [23, 24]. The block length of an original experiment is 30 sec-on and 30 sec-off. However, in order to separate the fundamental frequency of stimulus function from the low frequency noisy region distinctly, we shortened the block length as 12 sec-on and 9 sec-off. The experiment consisted of 16 task epochs (8 epochs for 2-back, 8 epochs for 0-back) and 16 rest epochs. During task period, a random series of single-digit numbers (1-9) was presented at the rate of one number every 2 sec. During 2-back task, subjects were instructed to press a key when each digit is same as the one presented two digits previously in the series.

5.4 Results

To evaluate the practical usefulness of proposed methods, we applied our new statistical analysis framework to right finger tapping and working memory experiment data. In spatial preprocessing step, the position of optodes in 3-D digitizer's real coordinate were accurately converted onto the position of the cortical cortex which is obtained from the segmented MR images. Figures 5.2(a) and (b) show the holder cap of optodes onto subject's scalp and 24 NIRS channels onto the SPM brain template, respectively.

In temporal preprocessing step, detrending based on DCT basis set was applied in NIRS data. In Figs. 5.3, red lines denote the estimated bias based on DCT basis, and blue lines correspond to the NIRS and fMRI time series. Estimated bias follows the trend of NIRS and fMRI signal well, as shown in Figs. 5.3 (a) and (b), respectively. Note that the signal

to noise ratio (SNR) of NIRS is very poor, compared with SNR of fMRI.

Now, we mainly focus on three points: 1) comparision with the GLM results from the "pre-coloring" and "pre-whitening" methods, 2) inference based on a new theory using Sun's tube formula that allows the super-resolution localization of brain activation, 3) consistency of NIRS and fMRI results.

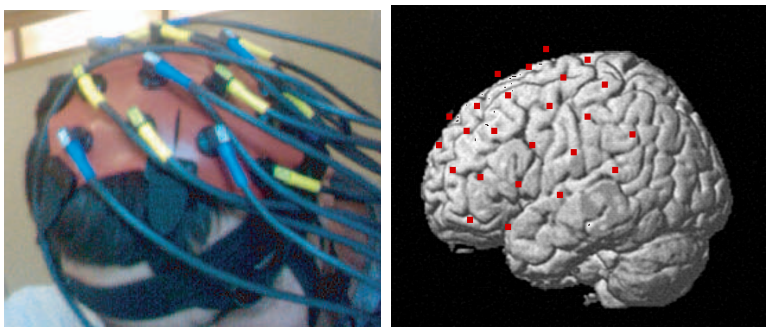

(a) (b)

Figure 5.2: (a) The holder cap of 16 optodes covering the primary motor cortex and Broca's area, (b) 24 NIRS channels onto the SPM brain template.

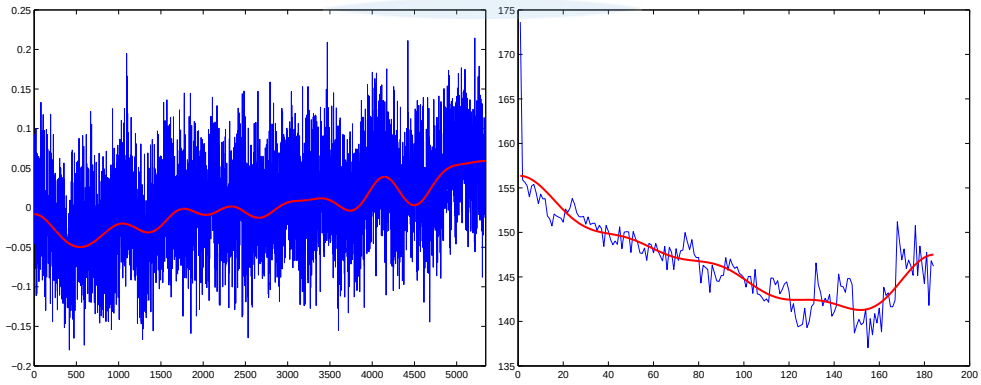

(a) (b)

Figure 5.3: Estimated trend of (a) NIRS and (b) fMRI signal. Blue line: (a) NIRS and (b) fMRI time series, red line: the estimated bias based on the DCT method.

5.4.1 Right Finger Tapping

T-statistic maps from ΔHbO_2 are shown in Figs. 5.4. T-statistic maps using fOSA [7] are shown in Figs. 5.4(a) and (b). Note that fOSA cannot analyze the the intepolated random field, so the block average T-maps are obtained. Our T-statistic maps using NIRS-SPM are shown in Figs. 5.4(c) and (d). Note that NIRS-SPM obtains the super-resolution T-maps, compared to fOSA results. Furthermore, the activation patterns which have relatively high T-values are more realistic than that of fOSA.

On the one hand, Figs. 5.4(a) and (c) show T-statistic maps from the pre-whitened ΔHbO_2. Figures 5.4(b) and (d) show T-statistic maps from the pre-colored ΔHbO_2. T maps from pre-colored ΔHbO_2 are more focused on the primary motor cortex that is the target region of finger tapping task.

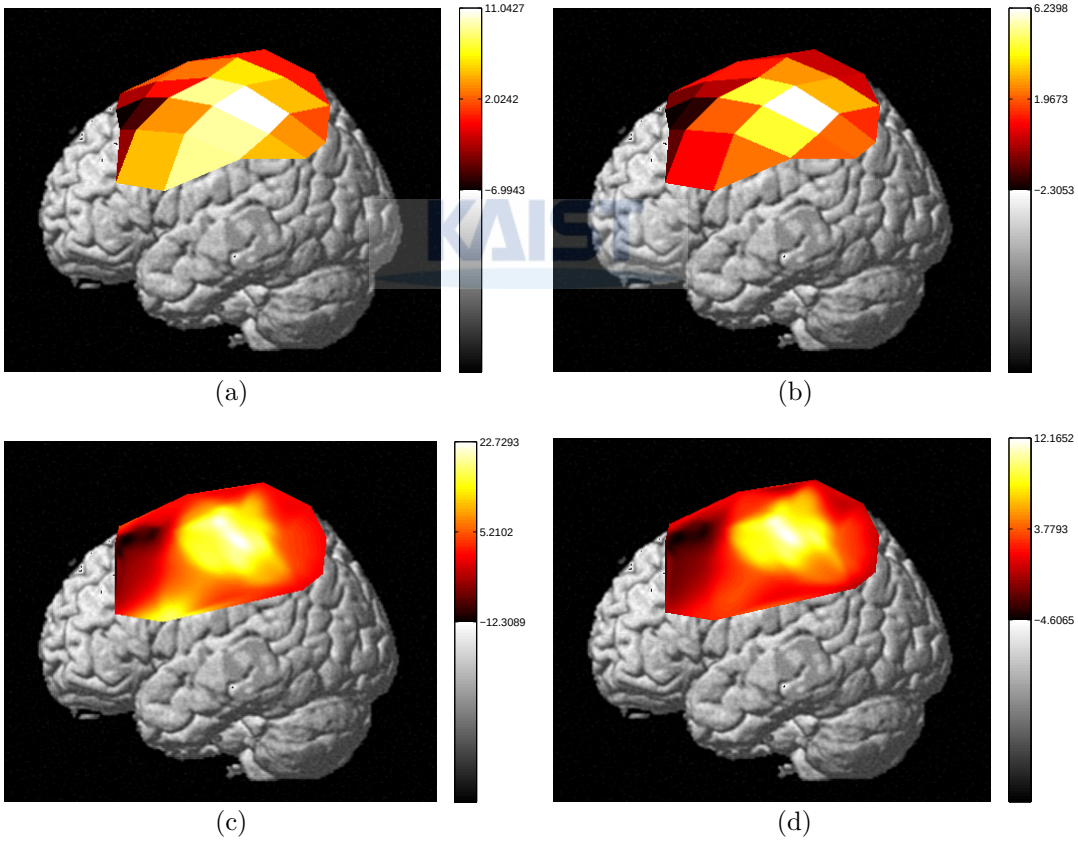

(a) (b)

(c) (d)

Figure 5.4: T-statistic maps from ΔHbO_2 using (a) pre-whitening, fOSA [7], (b) pre-coloring, fOSA, (c) pre-whitening, NIRS-SPM, and (d) pre-coloring, NIRS-SPM.

Figures. 5.5 and 5.6 show the T-statistic maps from ΔHbR and both ΔHbO_2 and ΔHbR, respectively. Again, NIRS-SPM obtains the high resolution T-statistic maps over the fOSA. Pre-coloring method allows that T-maps are more focused on the primary motor cortex than pre-whitening method.

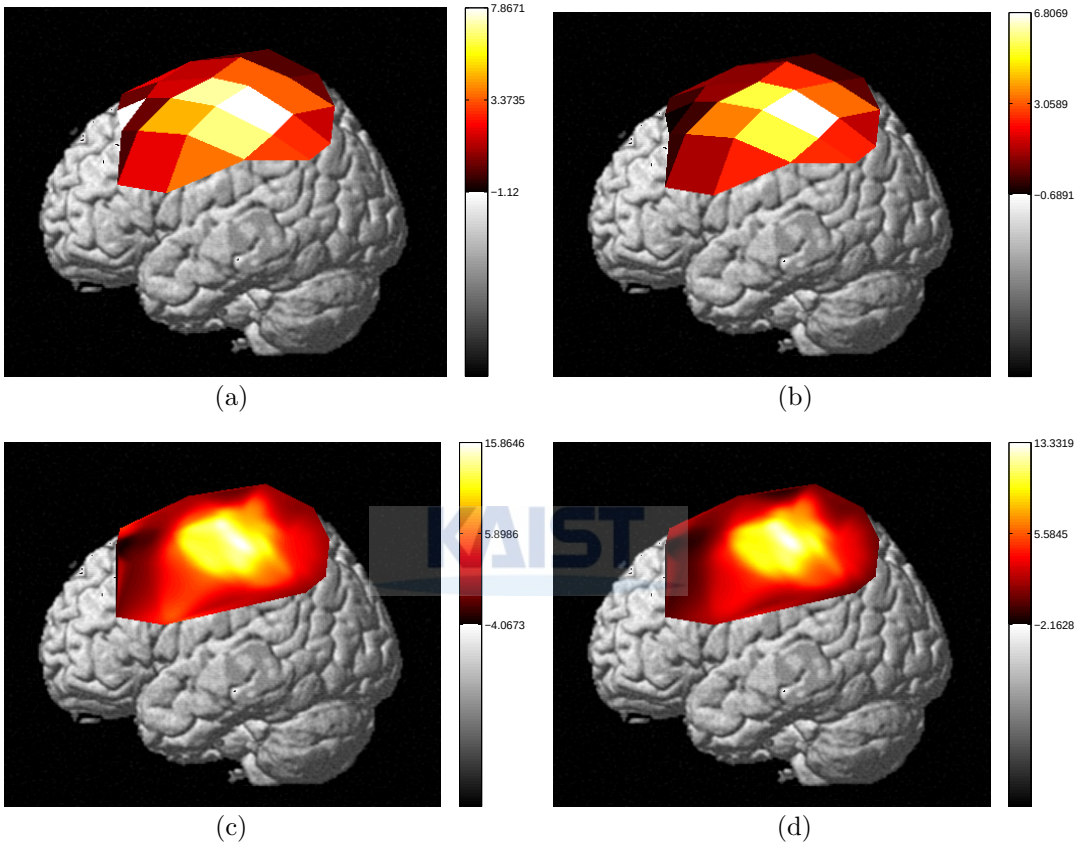

Figure 5.5: T-statistic maps from ΔHbR using (a) pre-whitening, fOSA, (b) pre-coloring, fOSA, (c) pre-whitening, NIRS-SPM, and (d) pre-coloring, NIRS-SPM.

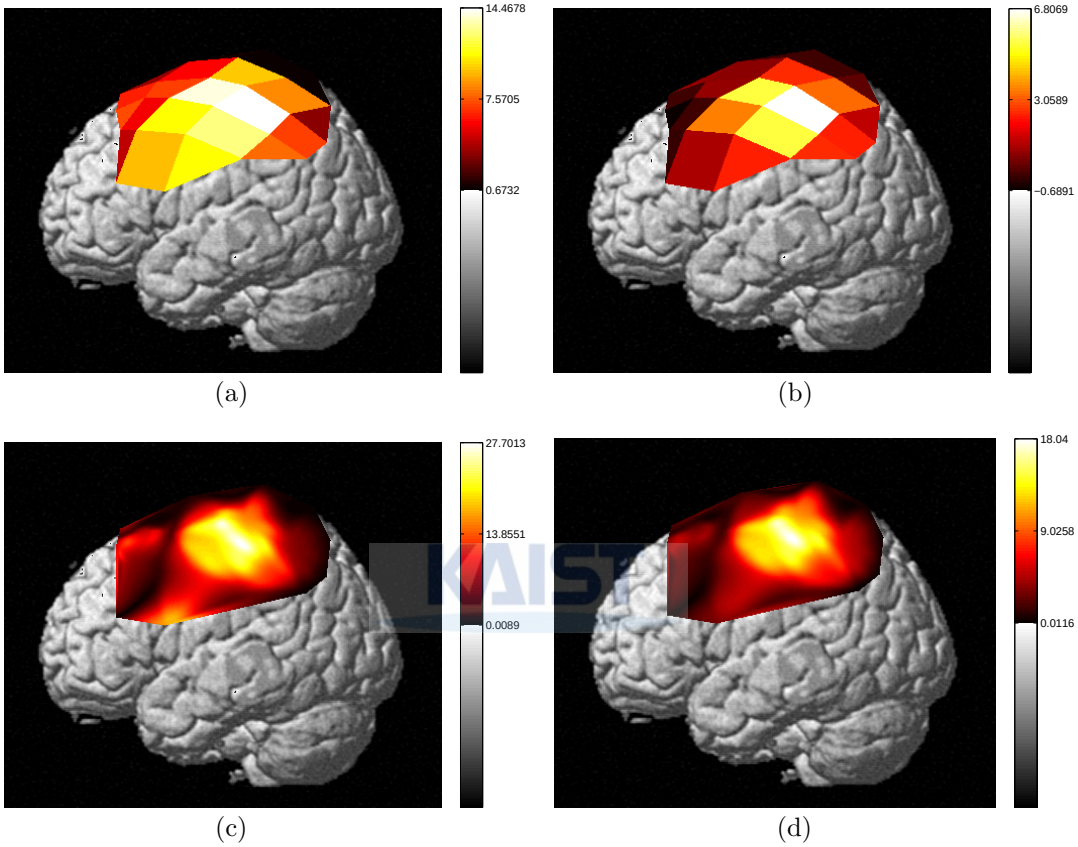

Figure 5.6: T-statistic maps from both ΔHbO_2 and ΔHbR using (a) pre-whitening, fOSA, (b) pre-coloring, fOSA, (c) pre-whitening, NIRS-SPM, and (d) pre-coloring, NIRS-SPM.

During the finger tapping task, fMRI data were simultaneously recorded with NIRS data. Figure 5.7 shows the activation pattern of BOLD signal. Activated area of BOLD signal is localized in the primary motor cortex very tightly.

Figures 5.8 show the activation area of ΔHbO_2. The activation maps using fOSA with Gaussian random field theory are shown in Figs. 5.8 (a) and (b). Since fOSA analyzes the block average T-map, the estimated activation areas are very rough. Activation maps using incomplete gamma bound and Sun's tube formula are shown in Figs. 5.8(c)(d) and (e)(f), respectively. Note that thresholds from incomplete gamma bound are higher than thresholds from Sun's tube formula.

From an autocorrelation estimation's point of view, Figs. 5.8(a)(c)(e) and (b)(d)(f) describe activation maps from pre-whitened and pre-colored ΔHbO_2, respectively. Note that activated area using pre-colored ΔHbO_2 are clearly focused on the primary motor cortex and fairly consistent with activation region of BOLD signal, as shown in Figs. 5.7. The incomplete gamma bound gives very optimistic estimate of the activated area, whereas the tube formula tells us that the more areas are activated by the finger tapping. Both of the results exhibit excellent correlation with the fMRI result.

Figures. 5.9 and 5.10 show the activation maps from ΔHbR and both ΔHbO_2 and ΔHbR, respectively. Again, NIRS-SPM obtains the super-resolution activated region, compared to fOSA. Activation area using pre-coloring method are more focused on the primary motor cortex than pre-whitening method.

KAIST

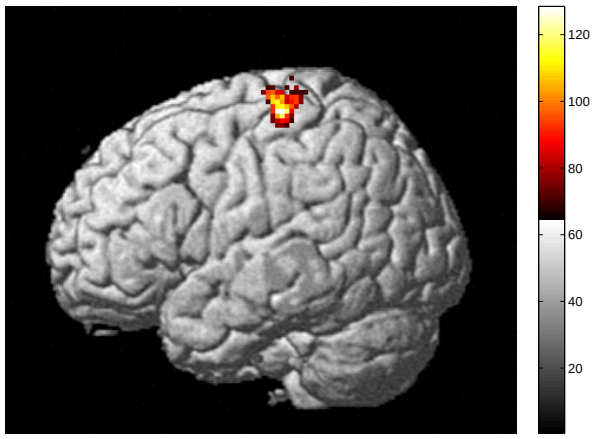

Figure 5.7: SPM analysis of fMRI data (p-value < 0.01).

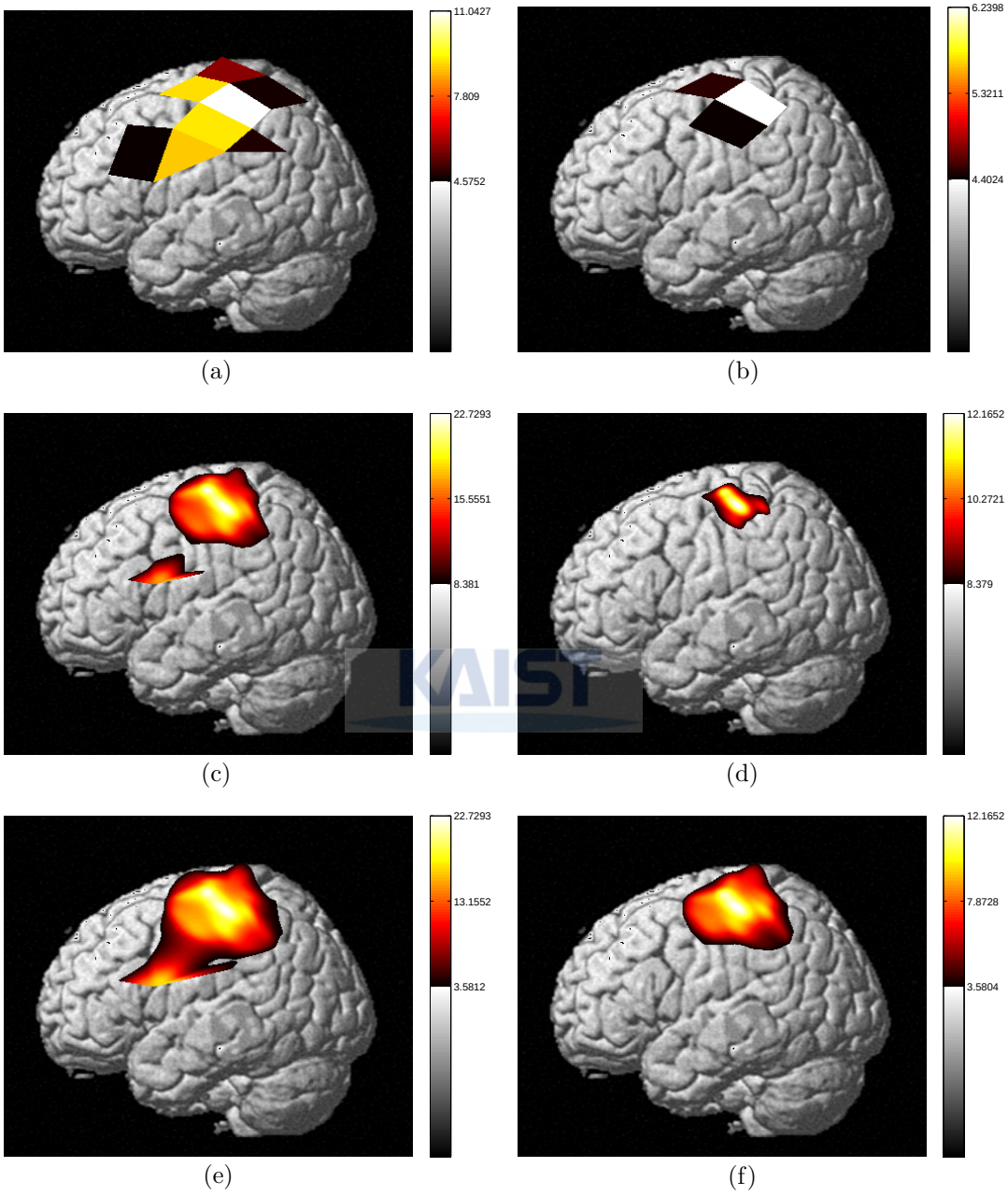

Figure 5.8: Activation area from ΔHbO_2 using (a) pre-whitening, fOSA, (b) pre-coloring, fOSA, (c) pre-whitening, incomplete gamma bound, (d) pre-coloring, incomplete gamma bound, (e) pre-whitening, tube formula, and (f) pre-coloring, tube formula.

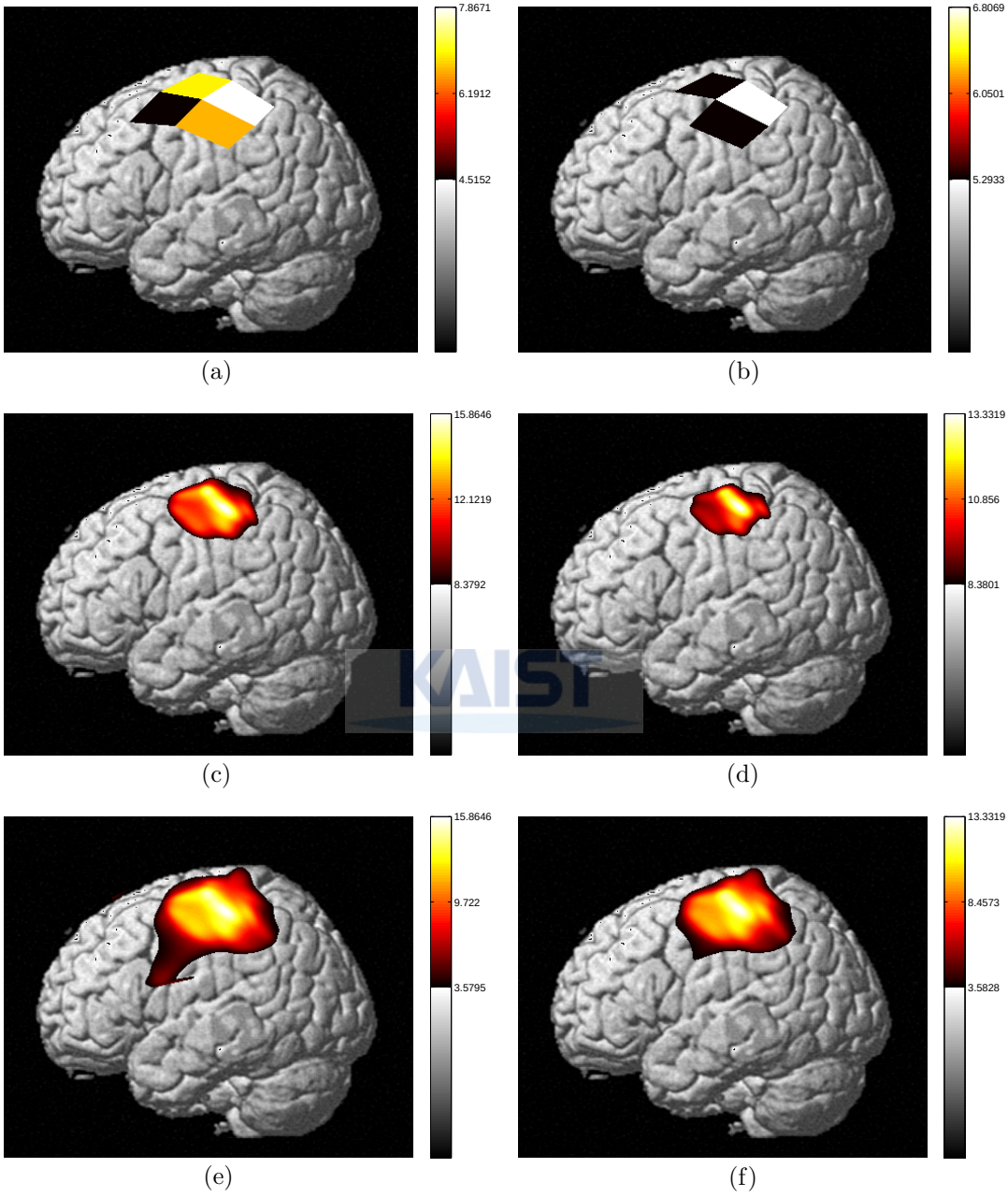

Figure 5.9: Activation area from ΔHbR using (a) pre-whitening, fOSA, (b) pre-coloring, fOSA, (c) pre-whitening, incomplete gamma bound, (d) pre-coloring, incomplete gamma bound, (e) pre-whitening, tube formula, and (f) pre-coloring, tube formula.

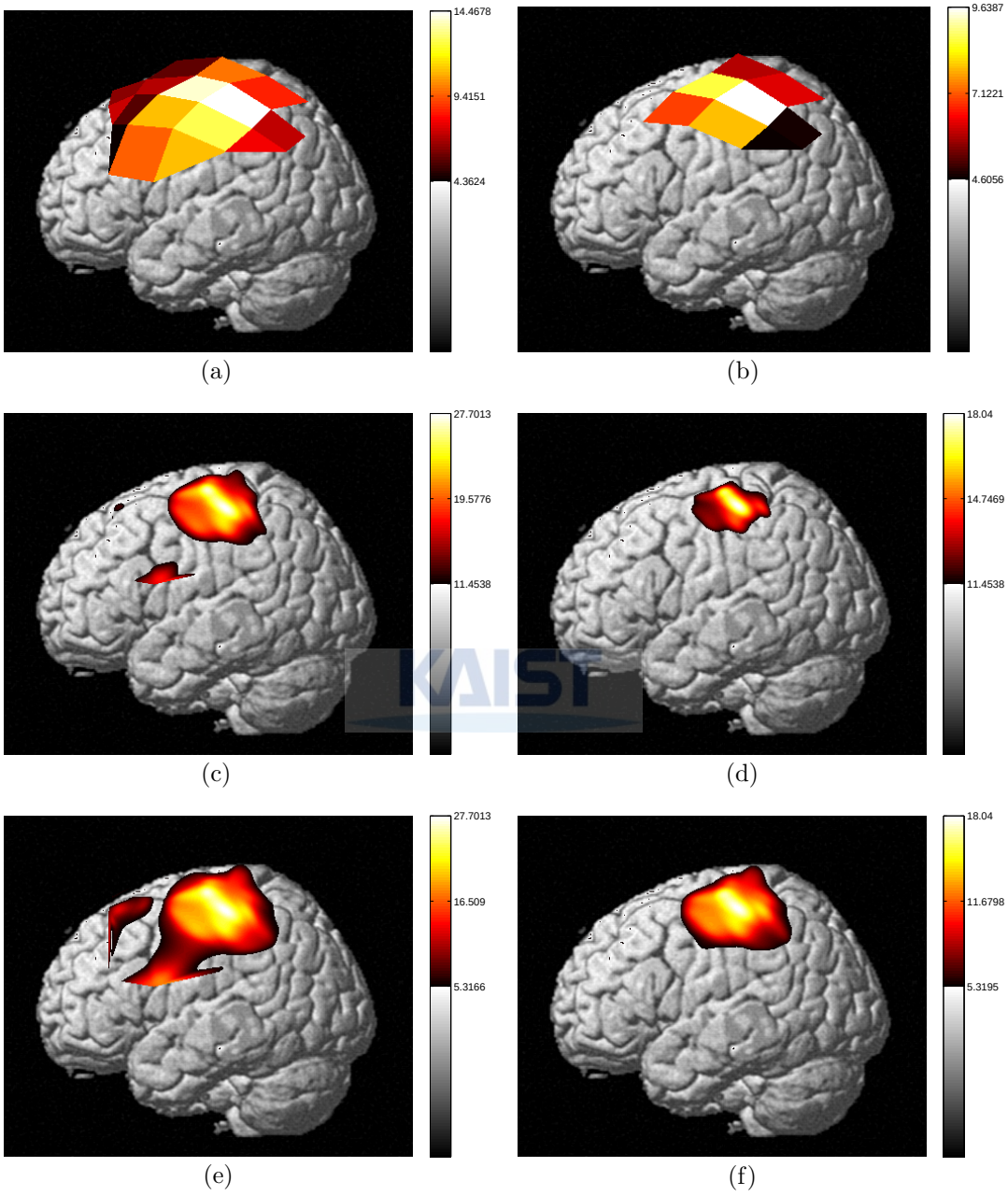

Figure 5.10: Activation area from both ΔHbO_2 and ΔHbR using (a) pre-whitening, fOSA, (b) pre-coloring, fOSA, (c) pre-whitening, incomplete gamma bound, (d) pre-coloring, incomplete gamma bound, (e) pre-whitening, tube formula, and (f) pre-coloring, tube formula.

5.4.2 Working Memory Task

T-statistic maps from ΔHbO_2 are shown in Figs. 5.11. T-statistic maps using fOSA are shown in Figs. 5.11(a) and (b). Note that fOSA cannot analyze the the intepolated random field, so the block average T-maps are obtained. Our T-statistic maps using NIRS-SPM are shown in Figs. 5.11(c) and (d). Note that NIRS-SPM obtains the super-resolution T-maps, compared to fOSA results. Furthermore, the activation patterns which have relatively high T-values are more realistic than that of fOSA.

From the autocorrelation estimation's point of view, Figs. 5.11(a) and (c) show T-statistic maps from the pre-whitened ΔHbO_2. Figures 5.11(b) and (d) show T-statistic maps from the pre-colored ΔHbO_2. T maps from pre-colored ΔHbO_2 are more focused on the Broca's area that is the target region of working memory task.

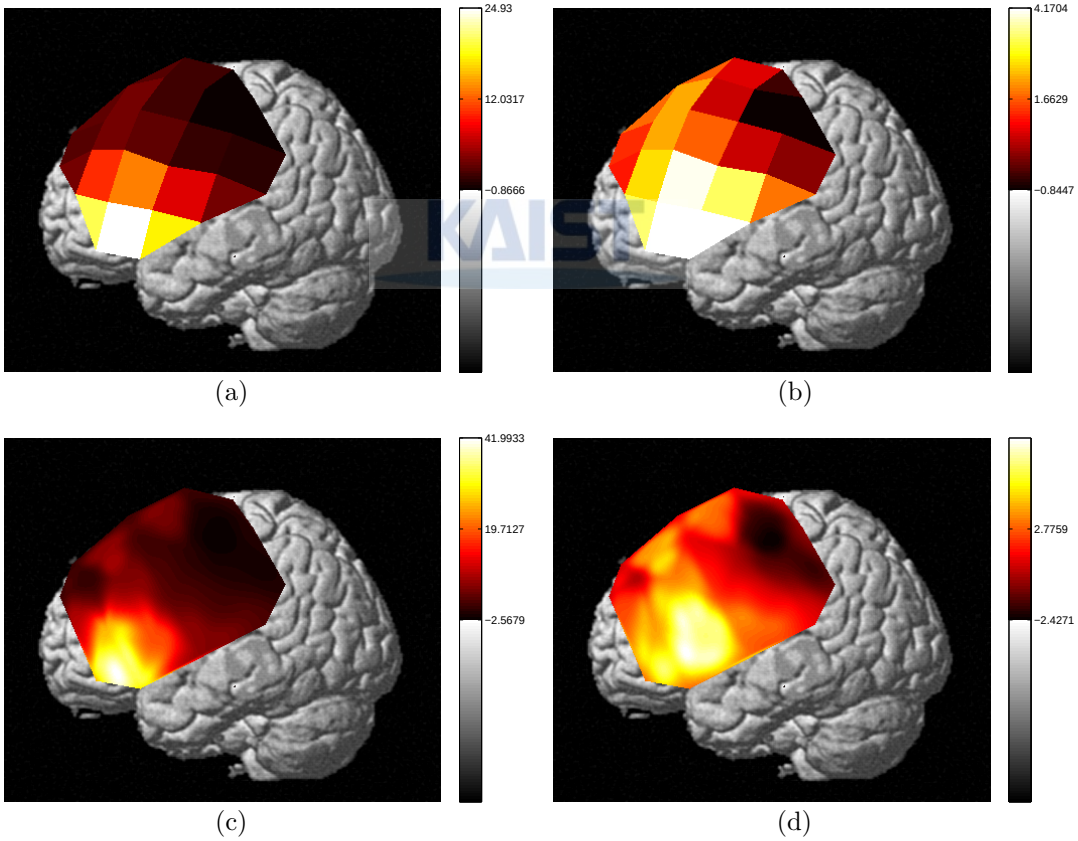

(a) (b)

(c) (d)

Figure 5.11: T-statistic maps from ΔHbO_2 using (a) pre-whitening, fOSA, (b) pre-coloring, fOSA, (c) pre-whitening, NIRS-SPM, and (d) pre-coloring, NIRS-SPM.

Figures. 5.12 and 5.13 show the T-statistic maps from ΔHbR and both ΔHbO_2 and ΔHbR, respectively. Again, NIRS-SPM obtains the high resolution T-statistic maps over the fOSA. Pre-coloring method allows that T-maps are more focused on Broca's area than pre-whitening method.

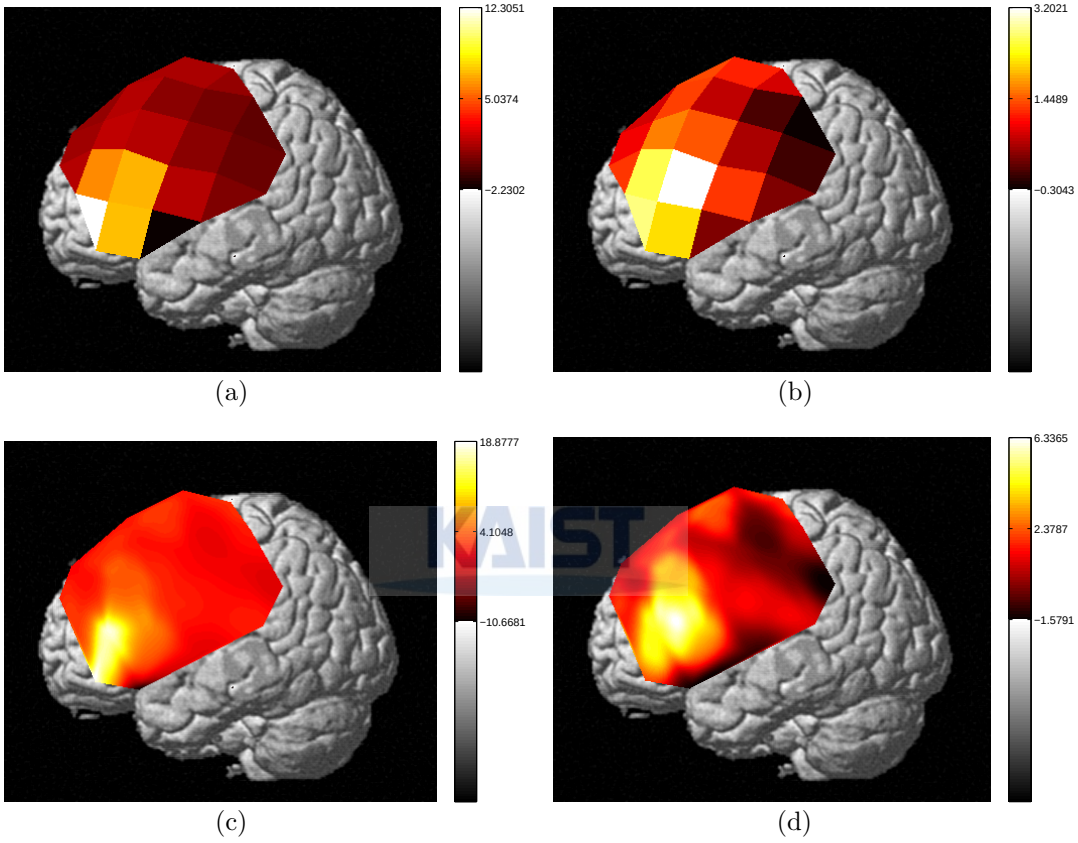

Figure 5.12: T-statistic maps from ΔHbR using (a) pre-whitening, fOSA, (b) pre-coloring, fOSA, (c) pre-whitening, NIRS-SPM, and (d) pre-coloring, NIRS-SPM.

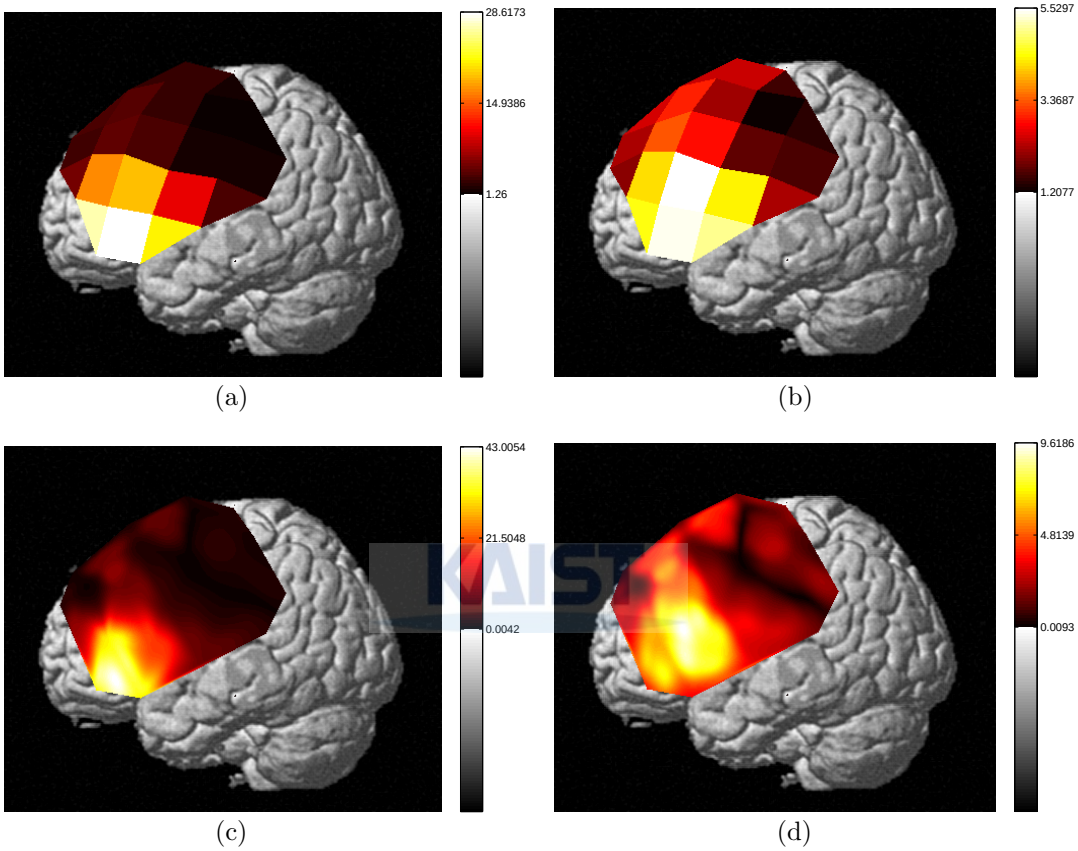

Figure 5.13: T-statistic maps from both ΔHbO_2 and ΔHbR using (a) pre-whitening, fOSA, (b) pre-coloring, fOSA, (c) pre-whitening, NIRS-SPM, and (d) pre-coloring, NIRS-SPM.

During the working memory task, fMRI data were simultaneously recorded with NIRS data. Figure 5.14 shows the activation pattern of BOLD signal. Figures 5.15 show the activation area of ΔHbO_2. The activation maps using fOSA with Gaussian random field theory are shown in Figs. 5.15 (a) and (b). Since fOSA analyzes the block average T-map, the estimated activation areas are very rough. Activation maps using Sun's tube formula are shown in Figs. 5.15(c)(d).

From an autocorrelation estimation's point of view, Figs. 5.15(a)(c) and (b)(d) describe activation maps from pre-whitened and pre-colored ΔHbO_2, respectively. Note that activated area using pre-colored ΔHbO_2 are clearly focused on Broca's area.

Figures. 5.16 and 5.17 show the activation maps from ΔHbR and both ΔHbO_2 and ΔHbR, respectively. Again, NIRS-SPM obtains the super-resolution activated region, compared to fOSA. Activation area using pre-coloring method are more focused on Broca's area than pre-whitening method.

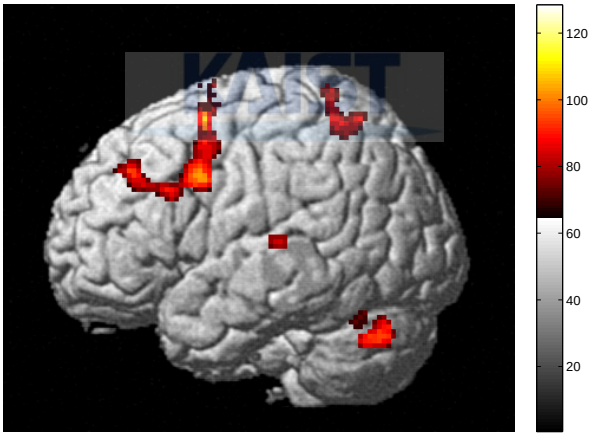

Figure 5.14: SPM analysis of fMRI data (p-value < 0.01).

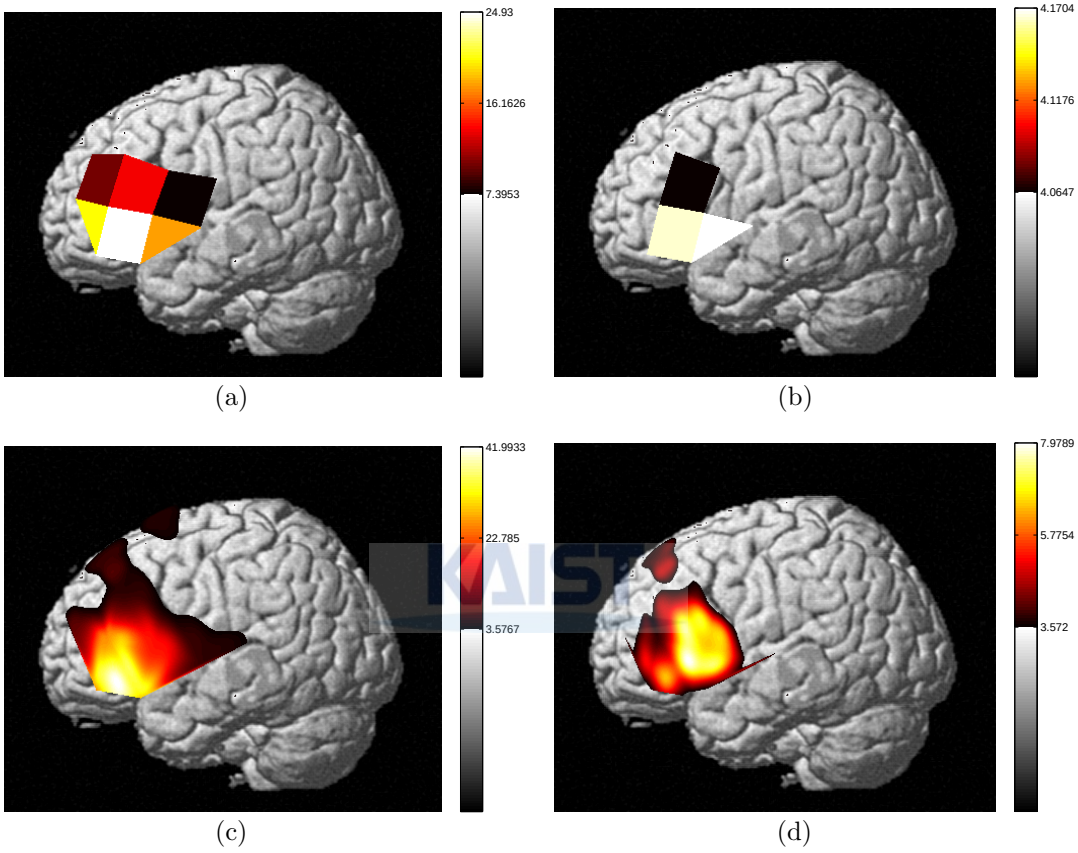

Figure 5.15: Activation area from ΔHbO_2 using (a) pre-whitening, fOSA, (b) pre-coloring, fOSA, (c) pre-whitening, tube formula, and (d) pre-coloring, tube formula.

In this section, we demonstrated that pre-coloring method is superior to pre-whitening method for temporal correlation estimation. There are several reasons that pre-coloring is more appropriate method for NIRS than pre-whitening method. First, sufficient temporal smoothing of pre-coloring method is essentially needed in NIRS time series. NIRS data which are simultaneously recorded with fMRI have very low SNR, as shown in Figs. 5.3(a). Relatively long optical fibers which connect the optode and NIRS equipment in MRI control room introduce the significant signal attenuation. Thus, in order to improve SNR, sufficient temporal smoothing is necessary in preprocessing step. In pre-whitening method,

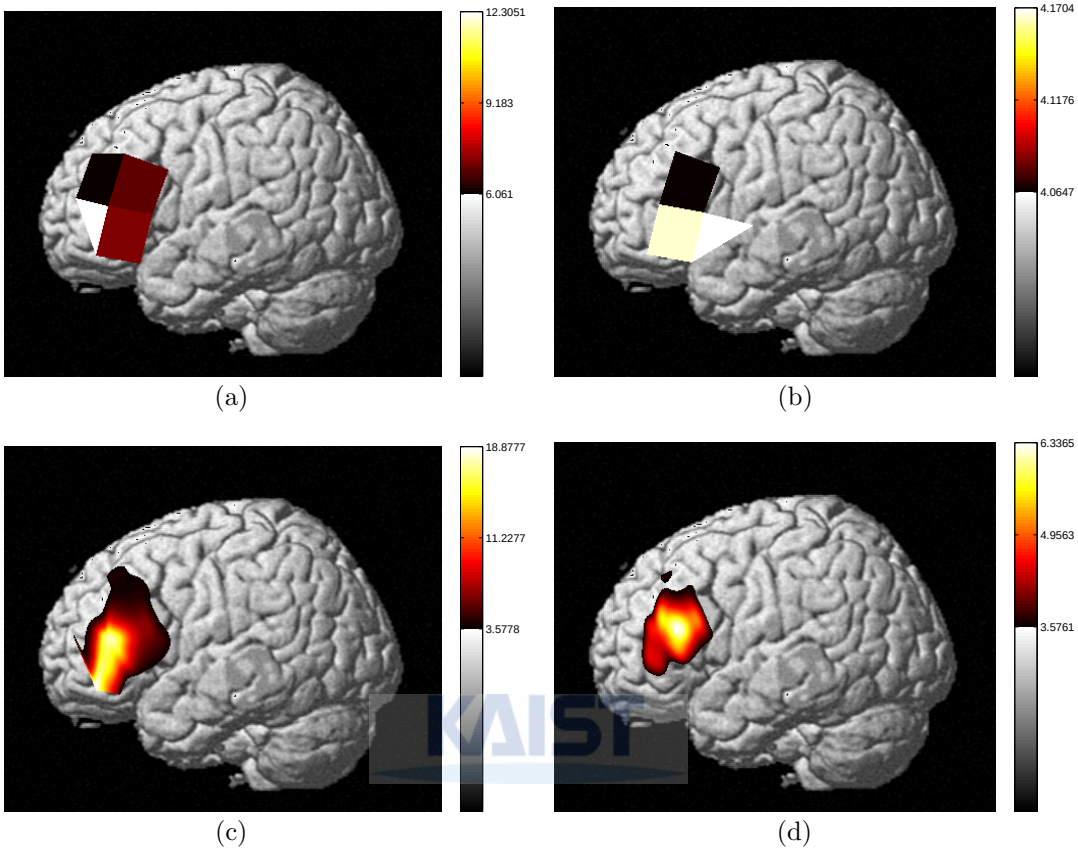

Figure 5.16: Activation area from ΔHbR using (a) pre-whitening, fOSA, (b) pre-coloring, fOSA, (c) pre-whitening, tube formula, and (d) pre-coloring, tube formula.

the intrinsic temporal correlation is estimated using unsmoothed NIRS data which have poor SNR. These increase the probability that pre-whitening produces some bias, due to the difference between estimated and actual temporal correlations. Second, pre-coloring method obtains the temporal correlation without ReML method. In ReML employed in pre-whitening method, the precision of hyperparameter estimates increases linearly with the number of measurements[12]. Because the number of measurements in NIRS data is much smaller than in fMRI data, it is not accurate to estimate the intrinsic temporal correlation using ReML. Furthermore, due to the computational burden of ReML, it takes much time to obtain the estimated temporal correlation. Based on these observations, pre-coloring method is more appropriate to NIRS data than pre-whitening method.

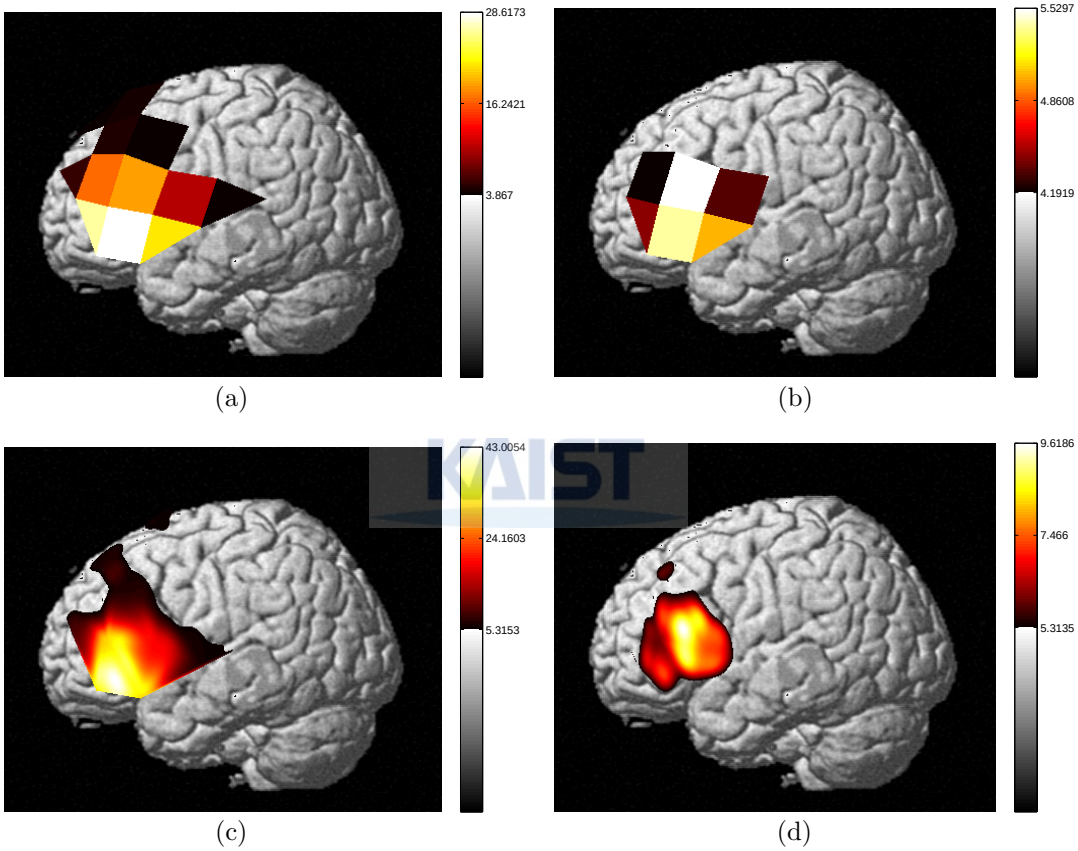

Figure 5.17: Activation area from both ΔHbO_2 and ΔRusing (a) pre-whitening, fOSA, (b) pre-coloring, fOSA, (c) pre-whitening, tube formula, and (d) pre-coloring, tube formula.

6. Conclusion

We developed a new public domain statistical toolbox called NIRS-SPM. In the main framework, NIRS-SPM successfully analyzed the NIRS data using GLM and calculated the p-value as the excursion probability which came from inhomogeneous Gaussian random field that are interpolated from the sparse measurement. In estimating the temporal correlation of NIRS, we demonstrated that pre-coloring method was more appropriate to NIRS than pre-whitening method, due to the computational efficiency and sufficient temporal smoothing. In spatial preprocessing, NIRS-SPM accurately localized the NIRS signal onto the cerebral cortex of anatomical MR image using Horn's algorithm. Experimental results from right finger tapping and working memory task showed that the activation pattern of NIRS from our software was fairly consistent with that of fMRI. Furthermore, NIRS-SPM allowed super-resolution localization of activated area.

KAIST

요 약 문

근적외선 분광신호와 기능자기공명영상의 동시측정 및 통계처리를 위한 Statistical Parametric Mapping Toolbox 개발

본 논문은 근적외선 분광신호와 기능자기공명영상의 동시 측정 및 통계처리가 가능한 toolbox (NIRS-SPM) 를 개발하였다. NIRS-SPM은 general linear model을 사용하여 근적외선 분광신호를 통계적으로 분석하고, tube formula를 사용하여 inhomogeneous Gaussian random field의 excursion probabiliy를 계산함으로써 p-value를 구할 수 있도록 구현되었다. 기존의 NIRS 통계처리 프로그램 (fOSA)이 interpolation된 근적외선 분광신호를 분석할 수 없는 단점이 있는 반면, NIRS-SPM은 interpolating kerner을 고려한 representation manifold를 통해서 p-value를 구하기 때문에, interpolation된 근적외선 분광신호를 분석할 수 있었다. 동시 측정된 근적외선 분광신호와 기능자기공명영상의 분석을 위해, Horn의 알고리듬을 사용하여, 근적외선 분광신호의 채널을 MR 영상에 정확하게 매핑할 수 있었다. Temporal correlation 추정의 경우, 근적외선 분광신호의 낮은 SNR과 적은 수의 채널 때문에, pre-whitening 방법 보다는 pre-coloring 방법이 근적외선 분광신호에 더 적합함을 밝혔다. NIRS-SPM을 사용하여 분석한 finger tapping 및 working memory task의 결과는 근적외선 분광신호의 활성화 부분과 BOLD 신호의 활성화 부분이 거의 일치함을 보여주었다. 마지막으로, NIRS-SPM은 근적외선 분광신호의 고해상도 통계분석이 가능함을 보여주었다.

References

[1] A. Villringer and U. Dirnafl, "Coupling of brain activity and cerebral blood flow: basis of functional neuroimaging," *Cerebrovasc. Brain Metab. Rev.*, vol. 7, pp. 240-276, 1995.

[2] F. F. Jobsis, "Noninvasive, infrared monitoring of cerebral and myocardial oxygen sufficiency and circulatory parameters," *Science*, vol. 198, pp. 1264-1267, 1977.

[3] R. W. Homan, J. Herman, and P. Purdy, "Cerebral location of international 10-20 system electrode placement," *Electroencephalogr. Clin. Neurophysiol.*, vol. 66, pp. 376-382, 1987.

[4] G. Strangman, J. P. Culver, J. H. Thompson, and D. A. Boas, "A quantitative comparison of simultaneous BOLD fMRI and NIRS recording during functional brain activation," *NeuroImage*, vol. 17, pp. 719-731, 2002.

[5] M. L. Schroeter, M. M. Bucheler, K. Muller, K. Uludag, H. Obrig, G. Lohmann, M. Tittgemeyer, A. Villringer, and D. Yves von Cramon, "Towards a standard analysis for functional near-infared imaging," *NeuroImage*, vol. 21, pp. 283-290, 2004.

[6] M. M. Plichta, S. Heinzel, A. C. Ehlis, P. Pauli, and A. J. Fallgatter, "Model-based analysis of rapid event-related functional near-infrared spectroscopy (NIRS) data: A parametric validation study," *NeuroImage*, vol. 35, pp. 625-634, 2007.

[7] P. H. Koh, D. E. Glaser, G. Flandin, S. Kiebel, B. Butterworth, A. Maki, D. T. Delpy, and C. E. Elwell, "Functional optical signal analysis: a software tool for near-infrared spectroscopy data processing incorporating statistical parametric mapping," *J. Biomed. Opt.*, vol. 12, pp. 1-13, 2007.

[8] K. J. Worsley and K. J. Friston, "Analysis of fMRI time-series revisited-again," *NeuroImage*, vol. 2, pp. 173-181, 1995.

[9] K. J. Friston, A. P. Holmes, J-B. Poline, C. J. Price, and C. D. Frith, "Dectecting activations in PET and fMRI: Levels of Inference and Power," *NeuroImage*, vol. 40, pp. 223-235, 1996.

[10] J. C. Ye, P. Moulin, and Y. Bresler, "Asymptotic global confidence regions for 3-D parametric shape estimation in inverse problems," *IEEE Trans. Image Process.*, vol. 15, pp. 2904-2919, 2006.

[11] J. Sun, "Tail probabilities of the maxima of gaussian random fields," *Ann. Prob.*, vol. 21, pp. 34-71, 1993.

[12] K. J. Friston, J. Ashburner, S. Kiebel, T. Nichols, and W. Penny, *Statistical Parametric Mapping: The analysis of functional brain images*, Academic Press, Sandiego, CA, USA, 2006.

[13] B.K.P. Horn, "Closed-form solution of absolute orientation using unit quaternions," *J. Opt. Soc. Amer. A*, vol. 4, pp. 629-642, 1987.

[14] K. J. Friston, C. D. Frith, P. F. Liddle, and R. S. Frackowiak, "Comparing function (PET) images: the assessment of significant change," *J. Cereb. Blood Flow Metab.*, vol. 11, pp. 690-699, 1991.

[15] R. N. A. Henson, C. J. Price, M. D. Rugg, R. Turner, and K. J. Friston, "Detecting latency differences in event-related BOLD responses: application to words versus nonwords and initial versus repeated face presentations," *NeuroImage*, vol. 15, pp. 83-97, 2002.

[16] G. M. Boynton, S. A. Engel, G. H. Glover, and D. J. Heeger, "Linear systems analysis of functional magnetic resonance imaging in human V1," *J. Neurosci.*, vol. 16, pp. 4207-4221, 1996.

[17] P. L. Purdon and R. M. Weisskoff, "Effect of temporal autocorrelation due to physiological noise and stimulus paradigm on voxel-level false-positive rates in fMRI," *Hum. Brain Mapp.*, vol. 6, pp. 239-249, 1998.

[18] K. J. Friston, W. D. Penny, C. Phillips, S. Kiebel, G. Hinton, J. Ashburner, "Classical and Bayesian inference in neuroimaging: theory," *NeuroImage*, vol. 16, pp. 465-483, 2002.

[19] K. J. Worsley, S. Marrett, P. Neellin, A. C. Vandal, K. J. Friston, and A. C. Evans, "A unified statistical approach for determining significant signals in images of cerebral activation," *Hum. Brain Mapp.*, vol. 4, pp. 58-73, 1996.

[20] M. Cope and D. T. Delpy, "System for long-term measurement of cerebral blood and tissue oxygenation on newborn infants by near infra-red transillumination," *Medical and Biological Engineering and Computing*, vol. 26, pp. 289-294, 1988.

[21] K. J. Friston, O. Josephs, E. Zarahn, A. P. Holmes, S. Rouquette and J-B. Poline, "To smooth or not to smooth? Bias and efficiency in fMRI time-series analysis," *NeuroImage*, vol. 12, pp. 196-208, 2000.

[22] G. A. Korn and T. M. Korn, *Mathematical Handbook for Scientists and Engineers*, McGraw Hill, New York, 1968.

[23] X. Wei, S. S. Yoo, C. C. Dickey, K. H. Zou, C. R. G. Guttmann, and L. P. Panych, "Functional MRI of auditory verbal working memory: long-term reproducibilit analysis," *NeuroImage*, vol. 21, pp. 1000-1008, 2004.

[24] E. E. Smith, J. Jonides, C. Marshuetz, and R. A. Koeppe, "Components of verbal working memory: Evidence from neuroimaging,", emphProc. Natl. Acad. Sci., vol. 95, pp. 876-882, 1998.

KAIST